CALIBRATION OF MICROBOLOMETER INFRARED CAMERAS FOR

MEASURING VOLCANIC ASH MASS LOADING

By

Russell C. Carroll

RECOMMENDED:

Dr. Denise Thorsen

Dr. Dejan Raskovic

Dr. Michael Hatfield

Dr. Joseph Hawkins
Advisory Committee Chair

Dr. Charlie Mayer
Chair, Department of Electrical and Computer Engineering

APPROVED:

Dr. Douglas Goering
Dean, College of Engineering and Mines

Dr. John Eichelberger
Dean of the Graduate School

8/15/14

Date

CALIBRATION OF MICROBOLOMETER INFRARED CAMERAS FOR MEASURING VOLCANIC ASH MASS LOADING

A

THESIS

Presented to the Faculty

of the University of Alaska Fairbanks

in Partial Fulfillment of the Requirements

for the Degree of

MASTER OF SCIENCE

By

Russell C. Carroll, B.S.

Fairbanks, Alaska

August 2014

Abstract

Small spacecraft with thermal infrared (TIR) imaging capabilities are needed to detect dangerous levels of volcanic ash that can severely damage jet aircraft engines and must be avoided. Grounding aircraft after a volcanic eruption may cost the airlines millions of dollars per day, while accurate knowledge of volcanic ash density might allow for safely routing aircraft around dangerous levels of volcanic ash. There are currently limited numbers of satellites with TIR imaging capabilities so the elapsed time between revisits can be large, and these instruments can only resolve total mass loading along the line-of-sight. Multiple small satellites could allow for decreased revisit times as well as multiple viewing angles to reveal the three-dimensional structure of the ash cloud through stereoscopic techniques. This paper presents the design and laboratory evaluation of a TIR imaging system that is designed to fit within the resource constraints of a multi-unit CubeSat to detect volcanic ash mass loading.

The laboratory prototype of this TIR imaging system uses a commercial off-the-shelf (COTS) camera with an uncooled microbolometer sensor, two narrowband filters, a black body source and a custom filter wheel. The infrared imaging system detects the difference in attenuation of volcanic ash at 11 μm and 12 μm by measuring the brightness temperature at each band. The brightness temperature difference method is used to measure the column mass loading. Multi-aspect images and stereoscopic techniques are needed to estimate the mass density from the mass loading, which is the measured mass per unit area.

Laboratory measurements are used to characterize the noise level and thermal stability of the sensor. A calibration technique is developed to compensate for sensor temperature drift. The detection threshold of volcanic ash density of this TIR imaging system is found to be from 0.35 mg/m^3 to 26 mg/m^3 for ash clouds that have thickness of 1 km, while ash cloud densities greater than 2.0 mg/m^3 are considered dangerous to aircraft. This analysis demonstrates that a TIR imaging system for determining whether the volcanic ash density is dangerous for aircraft is feasible for multi-unit Cubesat platforms.

Table of Contents

Page

Page

Page

List of Figures

Page

Page

List of Tables

Page

List of Appendices

Chapter 1
Introduction

1.1 Threat of Volcanic Ash

The multi-billion dollar aircraft industry and the safety of airline passengers are put at risk whenever a volcanic eruption occurs. However, ignoring this volcanic ash puts the pilots, aircraft and passengers at risk of turbine engine failure. Of special concern is the aircraft cargo hub situated in Alaska which is very near active volcanoes. Stopping this air traffic completely after an eruption can costs millions of dollars every day, such as the volcanic eruption over Europe in 2010 that cost the airline industry nearly two billion dollars over six days [1]. The 1989-1990 eruptions of the Redoubt volcano in Alaska cost the airline industry over 100 million dollars [2]. Currently there is a great need to accurately measure the position of dangerous volcanic ash so that it can be avoided without grounding all commercial aircraft.

Volcanic ash can be detected using infrared (IR) cameras by measuring the attenuation of radiation by the ash cloud. Spectral filters are inserted in front of the camera to find the attenuation of the radiation at each wavelength. This spectral data is used to calculate the volcanic ash mass loading, or average mass per unit area seen from a satellite, at all pixels across the image scene. Both unmanned aircraft vehicles (UAVs) and small satellites can be equipped with these sensors to provide enough information to detect dangerous levels of volcanic ash.

1.2 Purpose

This document describes a lab bench demonstration of an infrared imaging system for volcanic ash detection that could be flown on small spacecraft or UAVs. An accurate calibration procedure of the IR camera is developed. The electrical design for a lab bench demonstration is presented and a basic mechanical structure is given but further work will be needed for a field test. In addition, theoretical models are used to estimate the volcanic ash mass loading and associated uncertainties of measurements made by the imaging system. Dangerous levels of volcanic ash can be detected by comparing the transmission of radiation at two separate spec-

tral bands. The results of this project will be useful for further development of IR imaging systems used in volcanic ash detection.

1.3 Supplementing Existing Satellite Instruments

There are four existing satellites that have IR imaging instruments used in the detection of volcanic ash. For example, the Landsat 8 satellite includes the Thermal Infrared Sensor (TIRS) that is used for measuring land temperatures at two spectral bands in the infrared [3]. Various spectral bands and resolution of each satellite instrument are shown below in Table 1.1 along with the proposed IR imaging system that will be discussed in this thesis. Note that the final spacial resolution of the instrument depends on the optical lens selected (25-35 mm) and the altitude of satellite orbit (600-800 km). If the imaging instrument is deployed in a UAV the spectral resolution will be decreased significantly to 20-30 m.

Table 1.1: Comparison of Existing Satellites IR Imaging Systems used for Volcanic Ash Detection

Satellite	**Lower Band**		**Upper Band**		**Spacial**
	Band #	**Wavelength**	**Band #**	**Wavelength**	**Resolution**
AVHRR/3 [4]	4	10.3-11.3 μm	5	11.5-12.5 μm	1 km
ASTER [5]	13	10.3-11.0 μm	14	11.0-11.7 μm	90 m
MODIS [6]	31	10.8-11.3 μm	32	11.8-12.3 μm	1 km
TIRS [3]	10	10.6-11.2 μm	11	11.5-12.5 μm	100 m
Proposed Instrument	1	10.8-11.1 μm	2	12.0-12.5 μm	300-550m

1.3.1 Multiple Viewing Angles

The major drawback of the existing satellites is that most images of volcanic ash clouds are at a single look angle, nadir, looking directly down at the cloud. By recording the volcanic ash cloud from various viewing angles a three-dimensional structure of the cloud can be calculated using stereoscopic or multi-aspect techniques. This technique is currently impossible with current satellites but will be

achieved with addition of more viewing angles.

1.3.2 Small Satellites

While a larger satellite will have higher performance, there are several advantages of using smaller satellites. Small satellites will have much lower individual costs and therefore several satellites can be deployed at once. Revist times using multiple satellites can cut the time required for a single satellite to a fraction. In addition, these satellites can be equipped with cameras to view the ash cloud from a side view to give information in three dimensions. Therefore small satellites will decrease the revisit time as well as allow for calculating the three dimensional structure of the ash cloud.

One implementation concept for a small satellite is a CubeSat as shown below in Figure 1.1. The CubeSat is a specification controlled by California Polytechnic State University and Stanford University and restricts the single unit CubeSat to be a 10 cm cube and weighing less than 1.33 kg [7]. However two cubes can be combined to create a two-unit CubeSat measuring 10 cm $\times$ 10 cm $\times$ 20 cm with a maximum total mass of 2.66 kg. An IR imaging system can potentially be developed to fit the resource requirements of a multiple unit CubeSat including space and power.

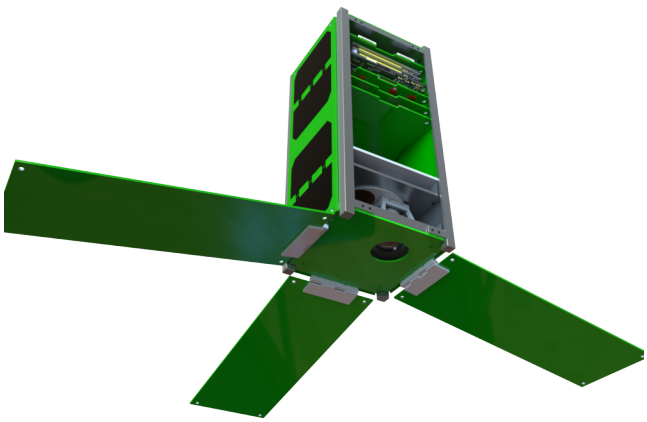

Figure 1.1: Potential Two-Unit CubeSat for IR Imaging (Courtesy Patrick Wade)

1.3.3 Unmanned Aircraft Vehicles

A UAV sweeping around the volcanic ash cloud will provide the ultimate control in viewing angle. With the UAV up close to the ash cloud a much higher resolution is given. This option is also very cost effective because a general purpose UAV can be used to carry the IR imaging module.

Two crucial disadvantages of using a UAV are as follows: limited altitude and regulations. Currently the regulations concerning the operation of UAVs are still being determined. However, imaging volcanic ash requires altitudes of at least 20 km and this is well beyond the ability of smaller UAVs. Therefore a high altitude UAV will be required, assuming the regulations allow it to fly at all.

1.3.4 High Altitude Balloons

High altitude balloons, also called near space balloons, are a simple solution to transporting the IR imager. A typical balloon can transport a mass of 2 kg to an altitude of 40 km, twice the required altitude. The major problem of a weather balloon is the lack of control over the balloon movement. Also, recovering the IR imager will be a challenge. However a high altitude balloon can be a potential transportation mode for a field demonstration of the IR imager.

1.3.5 Traditional Aircraft

Use of manned aircraft is definitely an option for carrying the IR module. The primary disadvantage is that the pilot and any passengers are put at risk due to the volcanic ash, especially when a jet engine is used. Propeller aircraft are also at risk to volcanic ash but have a reduced maximum altitude compared to jet engine aircraft. The required altitude of 20 km may be difficult to achieve. Therefore the use of manned aircraft should be used only if no alternative is found.

1.4 Path of Satellite Development

There will be three main steps in the development of the IR imaging system. The first is a lab bench demonstration that will provide the electrical interface to

the imaging system. Using this interface, the method for calibrating the imaging system will be developed. This step is achieved with this project.

The second step is to design the IR imaging system as a complete module that can be attached to a UAV, high altitude balloon or aircraft. This will include designing gimbals for stabilizing the imaging system and controlling the viewing direction. Most design work for this step will be mechanical in nature. This will conclude with a field test of the IR imager as illustrated below in Figure 1.2. If a volcanic ash cloud is not available the imager may be tested on smoke from forest fires or used for hot spot detection.

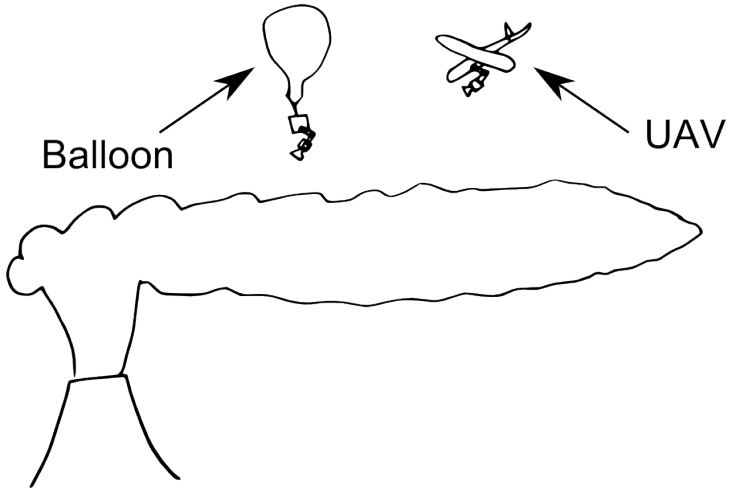

Figure 1.2: Field Test of IR Imager with Volcanic Ash

The final step is to create a prototype CubeSat with the imaging system. This will require a redesign of the electrical and mechanical components. A significant amount of systems engineering will be required to meet the tight constraints presented by using a CubeSat. An overview of the entire design process is given below in Table 1.2. This thesis project discusses only the first phase of the instrument development.

Table 1.2: Steps in Instrument Development

Development Phase	**Completed Hardware**	**Purpose**	**Date of Completion**
Lab Bench	Basic Demonstration (Electrical)	Develop Calibration Procedure	July 2014
Field Test	Prototype Module (Mechanical)	Verify Operation	Summer 2015
Satellite Demonstration	Operational CubeSat (Systems)	Observe Volcanic Ash	Summer 2018

1.5 Organization

This paper is organized in the following chapters:

Chapter 2 discusses the background science of volcanic ash cloud detection. The instrument dynamic range is calculated and a method is presented that shows a dangerous concentration of volcanic ash can be detected.

Chapter 3 is a review of the operation of bolometer detectors. There is a focus on the noise and uncertainty relationships between temperature and radiance.

Chapter 4 describes the essential components required for a thermal imaging system for detecting volcanic ash clouds. Integration into a module for a UAV interface is discussed.

Chapter 5 discusses the methods for calibrating a microbolometer infrared camera. Essential to the design is the on-board black body target for a reference.

Chapter 6 lists the basic requirements for the electrical interface to the FLIR Quark camera. This includes the electrical connector pin-out as well as the various commands that can be sent to the camera.

Appendix A gives the details of calculating the scattering efficiency of volcanic ash particles.

Appendix B presents the detailed calculations of estimating the volcanic ash and the related uncertainties.

Appendix C reviews the electronic system design of the control board. Required power supply improvements are included.

Chapter 2
Extinction of IR Radiation through Ash

2.1 Background

Detection of volcanic ash clouds using satellite IR sensors was originally performed by Prata in 1989 [8]. This consists of measuring the IR radiation at two separate wavelengths, calculating the equivalent black body temperature for this radiance, and taking the difference of these brightness temperatures. A brightness temperature difference (BTD) of negative values is usually indicative of volcanic ash while a positive BTD indicates a moisture cloud. This BTD generally decreases with decreased transmission at the lower wavelength.

Infrared imaging was first used by Prata in 1989 to differentiate dangerous volcanic ash clouds from harmless moisture clouds [8]. As shown below in Figure 2.1, the moisture and ash clouds have a similar transmission at 12 μm and can be called the reference value of transmission. Moisture clouds have a higher transmission at 11 μm while the volcanic ash clouds decrease in transmission at 11 μm. Therefore measuring the difference in transmission of a cloud at 11 and 12 μm will differentiate between a volcanic ash or moisture cloud. Note that this is a qualitative argument only but demonstrates the overall method used in ash cloud detection.

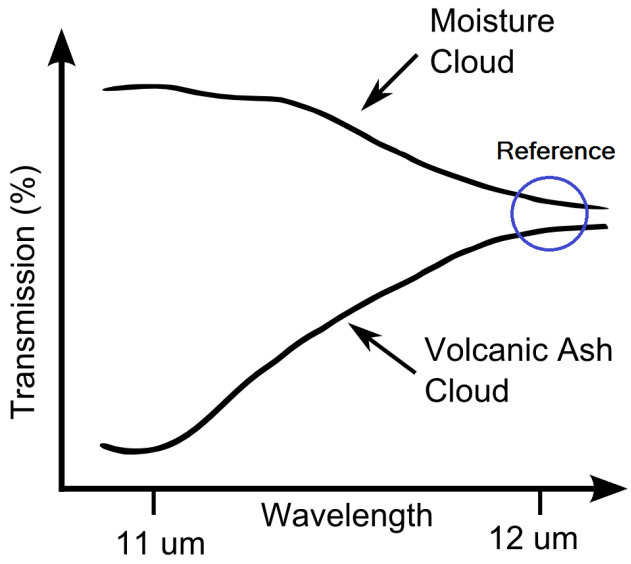

Figure 2.1: Sketch of Transmission Compared to Wavelength

However the transmission of infrared radiation is only part of the story. A complete analysis must take into account the scattering and absorption of the volcanic ash. The following will present a theoretical model of the ash cloud, how the radiance received by the sensor is calculated, and the method used for finding the properties of the cloud.

2.2 Theoretical Model of Volcanic Ash

A basic single slab model of the ash cloud is useful for calculating the total radiation that reaches the sensor. Some radiation will be from the earth that is attenuated by the ash cloud. The other source of radiation will be emission from the ash cloud.

The single slab model of the ash cloud in terms of radiance is shown below in Figure 2.2. The temperature of the ground T_g and temperature of the cloud T_c define the emitted radiance of the ground J_g and cloud J_c, respectively. Included is the transmitted radiance J_t, the reflected radiance J_r and the absorbed radiance αJ_g. Note that due to the conservation of energy in thermal equilibrium, the absorption α and emissivity ε of the cloud must be equal with $\alpha(\lambda) = \varepsilon(\lambda)$ for all wavelengths λ. A key result from this diagram is that the observed radiance from space is the sum of the transmitted radiance from the ground and the emitted radiance from the ash cloud.

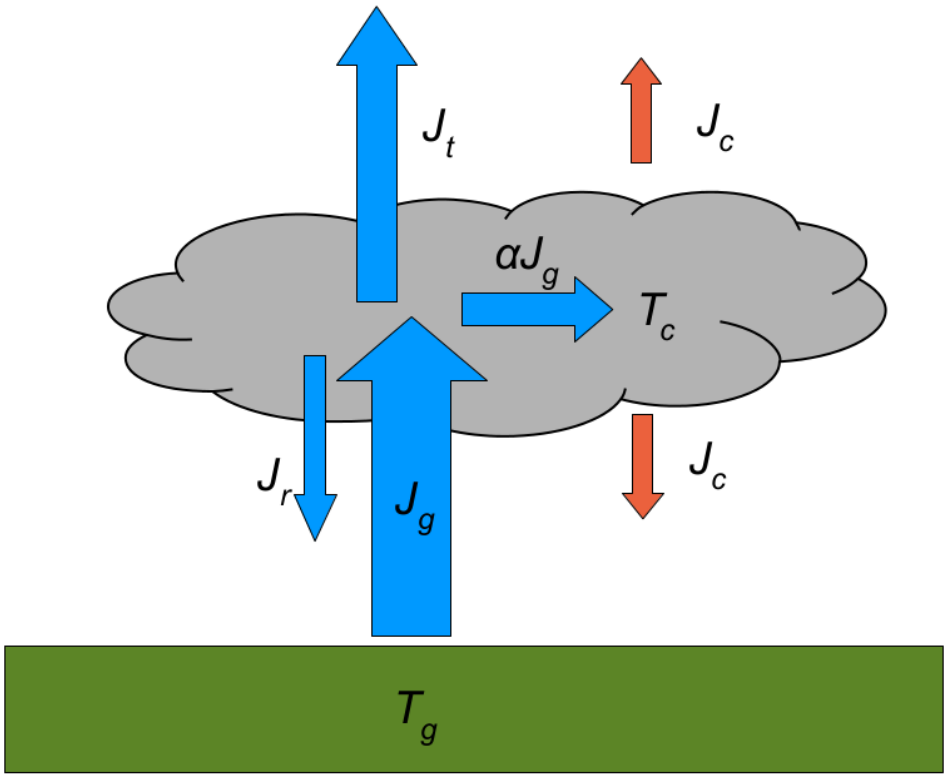

Figure 2.2: Single Slab Model of Ash Cloud

The single slab model shows the transfer of radiation from a conservation of energy perspective but does not require any specific spectral response. The total transmitted radiance shown in Figure 2.2 can be calculated by integrating across the spectrum as,

$$J_t = \int_0^\infty J_{t,\lambda} d\lambda. \tag{2.1}$$

Note that the above diagram does not take into account the attenuation of the atmosphere or the reflected radiance from the sun off of the ash cloud or earth. The atmosphere is expected to attenuate the IR radiation from the ground by 70% [9]. Scattered radiation from the sun is typically be ignored.

2.3 Transmission of IR Radiation

The purpose of this section is to find how much radiation will reach the sensor. First, the optical depth τ of the cloud can be estimated as shown below in Equation (2.2) with β_{ext} as the extinction coefficient, N as the particle density per unit volume, A as the geometric cross section area of the particle, and Δs as the effective volcanic ash cloud depth. The extinction efficiency Q_{ext} is used to find the effective cross section area of the particle $Q_{ext} \cdot A$ due to extinction of radiation through the cloud. Note that the extinction efficiency Q_{ext} is the sum of the absorption efficiency Q_{abs} and scattering efficiency Q_{sca} such that $Q_{ext} = Q_{abs} + Q_{sca}$. The optical response of the particle is represented as the extinction coefficient. For simplicity the particle density is assumed to be uniform throughout the ash cloud shown in Figure 2.2. The optical depth is found as

$$\tau = \int_{s_1}^{s_2} \beta_{ext}(s) \cdot ds = \int_{s_1}^{s_2} N \cdot A \cdot Q_{ext} \cdot ds = N \cdot A \cdot Q_{ext} \cdot \Delta s. \tag{2.2}$$

The optical depth is then used to calculate the transmitted spectral radiance $J_{t,\lambda}$ using Beer's law as shown below in Equation (2.3) with $J_{i,\lambda}$ as the incident surface spectral radiance,

$$J_{t,\lambda} = J_{i,\lambda} \cdot e^{-\tau} = J_{i,\lambda} \cdot e^{-N \cdot A \cdot Q_{ext} \cdot \Delta s}. \tag{2.3}$$

An IR detector from space would then observe the sum of the transmitted surface radiance as well as the radiance emitted by the ash cloud. In this simple single slab model the attenuation due to the atmosphere is ignored. Also, the effect of the ice or water particles is not included.

The spectral radiance $J_{BB,\lambda}$ of an ideal black body source, known as Planck's law, is given below in Equation (2.4) with h as Planck's constant, c as the speed of light, λ as the wavelength, k_B as Boltzmann's constant and T as the temperature of the black body,

$$J_{BB,\lambda}(T) = \frac{2hc^2}{\lambda^5} \frac{1}{e^{\frac{hc}{\lambda k_B T}} - 1}. \tag{2.4}$$

Using the above relation and Equation (2.3), the observed spectral radiance as seen by the sensor can be calculated as shown below with ε_g and ε_c being the emissivity of the ground and the cloud at the given wavelength and T_g and T_c being the temperature of the ground and cloud, respectively. This gives the observed spectral radiance to be

$$\begin{aligned} J_{sensor,\lambda} &= J_{t,\lambda} + J_{c,\lambda} = J_{g,\lambda} \cdot e^{-N \cdot A \cdot Q_{ext} \cdot \Delta s} + J_{c,\lambda} \\ &= \frac{2hc^2}{\lambda^5} \left[\frac{\varepsilon_g(\lambda) e^{-N \cdot A \cdot Q_{ext} \cdot \Delta s}}{e^{\frac{hc}{\lambda k_B T_g}} - 1} + \frac{\varepsilon_c(\lambda)}{e^{\frac{hc}{\lambda k_B T_c}} - 1} \right]. \end{aligned} \tag{2.5}$$

Note that the spectral radiance $J_{sensor,\lambda}$ is related to the observed radiance $J_{observed}$ by Equation (2.6), with $H(\lambda)$ being the spectral response of the IR camera system and λ_1 and λ_2 representing the half-power bandwidth of the spectral filter to give

$$J_{observed} = \int_{\lambda_1}^{\lambda_2} H(\lambda) \cdot J_{sensor,\lambda} \, d\lambda \approx H_{eff} \cdot (\Delta\lambda) J_{sensor,\lambda}. \tag{2.6}$$

Therefore the measured radiance depends on the response of the optical system. Attenuation due to the atmosphere can be included in the $H(\lambda)$ term.

2.4 Scattering and Absorption of Volcanic Ash

The first step to understanding the scattering and absorption of volcanic ash is to find the scattering and absorption efficiency of volcanic ash. Assuming a spherical particle of some effective radius, these efficiency values can be calculated from the index of refraction of the particle. The effective radius is the weighted average of the particle radius across the cross section distribution [10]. This is shown below in Equation 2.7 with $n(r)$ being the particle size distribution and gives

$$r_{eff} = \frac{\int \pi r^3 n(r) dr}{\int \pi r^2 n(r) dr}. \tag{2.7}$$

This paper will assume a uniform particle size distribution, with all particles having a physical radius equal to the effective radius. More realistic distributions in-

clude the modified gamma or log-normal distribution [10].

The scattering and absorption of volcanic ash particles can be calculated using the Mie scattering of a dielectric sphere with a specific refractive index. Complex refractive index values for water/ice as well as volcanic ash particles are shown below in Table 2.1 as given by Prata [11]. Volcanic ash will vary from one volcano to the next but the exact refractive index will not be critical to the calculated BTD, as found from an extensive parametric study by Wen and Rose [10].

Table 2.1: Refractive Index of Particulate Materials at 10.8 μm and 11.9 μm

Substance	$n_{(10.8\,\mu\text{m})}$	$n_{(11.9\,\mu\text{m})}$
Water	1.153 + i 0.097	1.111 + i 0.199
Ice	1.091 + i 0.168	1.258 + i 0.409
75% H_2SO_4	1.678 + i 0.301	1.844 + i 0.194
Quartz	1.940 + i 0.350	1.780 + i 0.190
Pumice	1.790 + i 0.370	1.800 + i 0.180

With an estimate of the index of refraction for pumice, the extinction coefficient can be calculated using the Mie scattering theory. The resulting extinction efficiency Q_{ext} is plotted for pumice shown below in Figure 2.3 and calculated using the Matlab script *Q_ideal.m* as discussed in Appendix A. These curves are equal at 3.5 μm and therefore the maximum effective radius for detection is about 3 μm when a uniform particle distribution is assumed. If scattering is ignored, the maximum effective particle radius is found to be 6.5 μm. However, this paper will assume that the maximum effective radius allowed for detection of the volcanic ash is 5 μm in order to correspond with values presented by Wen and Rose [10].

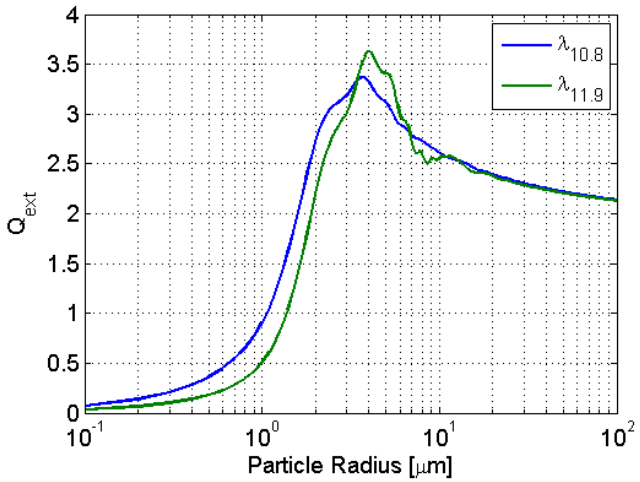

Figure 2.3: Extinction Efficiency for Various Pumice Particle Radii

With the optical properties of ash particles known, the transmission through an ash cloud can be calculated. Knowledge of the radiation transmission can now be used to predict the effective radius and optical depth of the ash cloud.

2.5 BTD Method

It is intuitive to convert spectral radiance into brightness temperature (BT). BT is defined as the equivalent black body temperature that gives the same spectral radiance. This BT is calculated by inverting the Planck function and applying to the measured spectral radiance. The difference in brightness temperature can then be plotted as shown in Figure 2.4 with and without ice particles. It is shown that small particles of effective radius 2 μm have a negative BTD while very large particles at 16 μm have a positive BTD. In contrast, when ice clouds are present and the fraction of ice particles to the total number of particles *fi* is at 0.5, the BTD still remains negative for an effective particle radius of 2 μm for the volcanic ash cloud. However, when the fraction of ice particles *fi* is increased to 0.7, the BTD curve is pushed into the positive BTD region. Therefore a certain amount of ice particles can be ignored. However, if the concentration of ice particles becomes too large the volcanic ash cloud will not be distinguishable from a moisture cloud because the BTD will become positive. Further, this method can never distinguish volcanic ash clouds with a large effective radius from moisture clouds because the BTD will be positive in both cases [8].

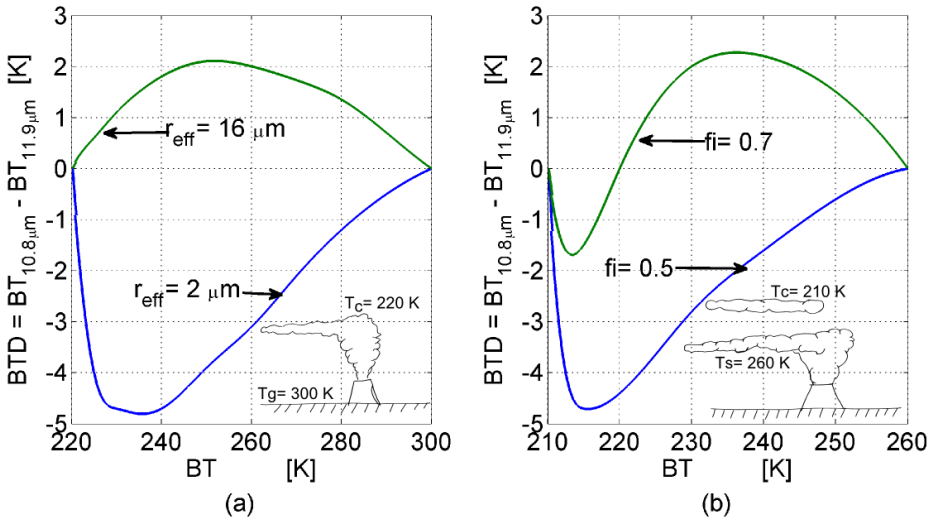

Figure 2.4: BTD without (a) and with (b) Ice Particles

In addition, the total optical depth will affect the calculated BTD as shown below in Figure 2.5. Note that as $\tau \to \infty$ the BTD approaches the cloud temperature. An optical depth of zero will correspond to the ground temperature. Ash clouds with a smaller particle radius will generally have a larger BTD and therefore will be easier to detect. Included is the effect of the surface temperature on the BTD from the surface temperature, with the magnitude of the BTD increasing as the surface temperature increases [10]. Therefore the magnitude of BTD will increase with an increase in ground temperature and/or a decrease in particle radius.

It is important to note from Figure 2.5 that the optical depth τ_o and the effective particle radius r_{eff} can both be interpolated. First, the measured BT at 10.8 μm will be measured with the IR camera and the X coordinate determined. Second, the measured BTD between the upper and lower bands will be used to find the Y coordinate. This X-Y coordinate will indicate a unique τ_o and r_{eff}.

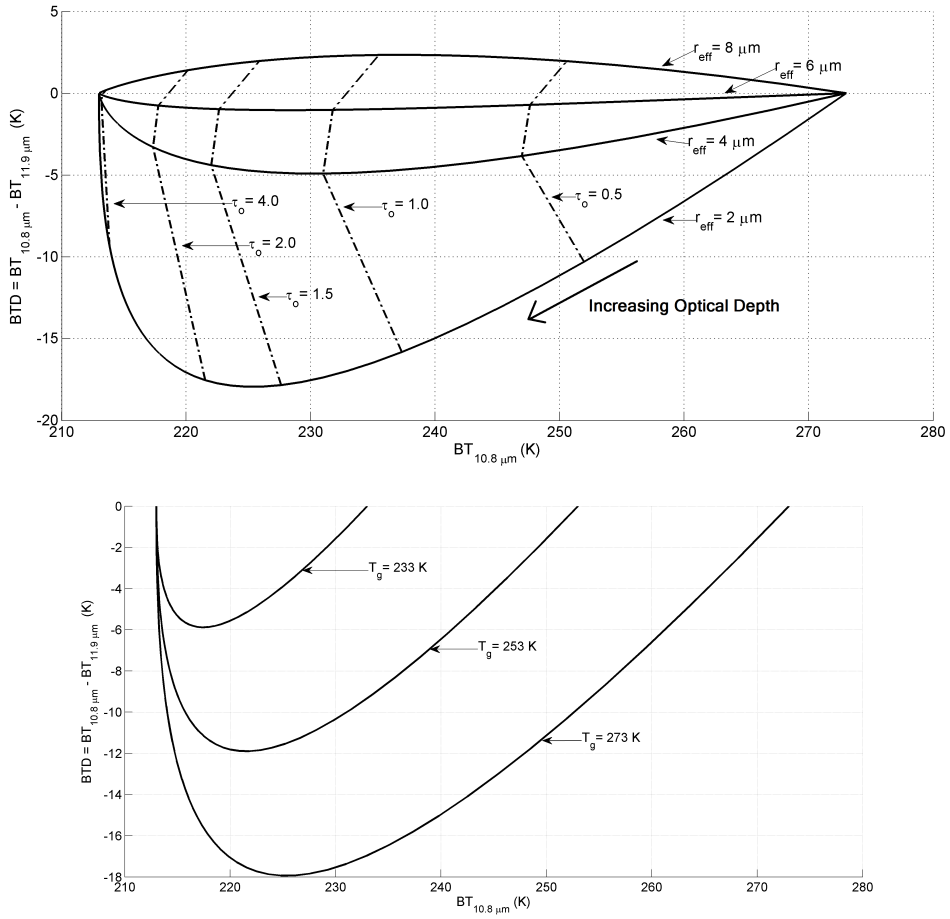

Figure 2.5: Effect of Optical Depth (Top) and Surface Temperature (Bottom) on Temperature Difference

Several assumptions must be made to produce the BTD chart shown above in Figure 2.5 including the ground temperature, the ground emissivity, the cloud temperature, the ash particle material, and the particle size distribution. From here measured brightness temperatures can be used to estimate the optical depth and effective particle radius. See Appendix B for more details on the analytic approach to calculating the optical depth and effective particle radius.

2.5.1 Particle Size Distribution

The effective particle radius distribution can be used to indicate whether assumptions about the volcanic ash cloud is valid. The top chart shown in Figure 2.6

shows all of the observed pixels of a volcanic ash cloud when plotted according to the measured BT and BTD. This volcanic ash data was presented by Wen [10]. A characteristic 'U' shape of the volcanic ash cloud is shown to lay along the line corresponding to a 3 μm effective particle radius. If the measured points did not lay along some effective radius line it would indicate that some assumptions about the ash cloud model are incorrect. This may include an incorrect index of refraction, physical particle size distribution $n(r)$, ground temperature or cloud temperature. These parameters should be adjusted as needed so that the 'U' curve of the cloud will lay along an line corresponding to an effective particle radius.

A plot of the frequency distribution of the effective particle radius was given by Wen [10] and shown below in Figure 2.6. Note that this is not the physical particle size distribution $n(r)$. Instead, the frequency that a given effective particle radius is measured using the BTD method is calculated using statistical methods. The measurements shown were made using AVHRR, with the measurements following the 'U' shape corresponding to an average effective particle radius of 3.0 μm. This means that each pixel is most likely to detect an effective particle size of 3.0 μm. A very wide distibution in the frequency distribution of the effective particle size will likely indicate that assumptions about the volcanic ash cloud model is incorrect.

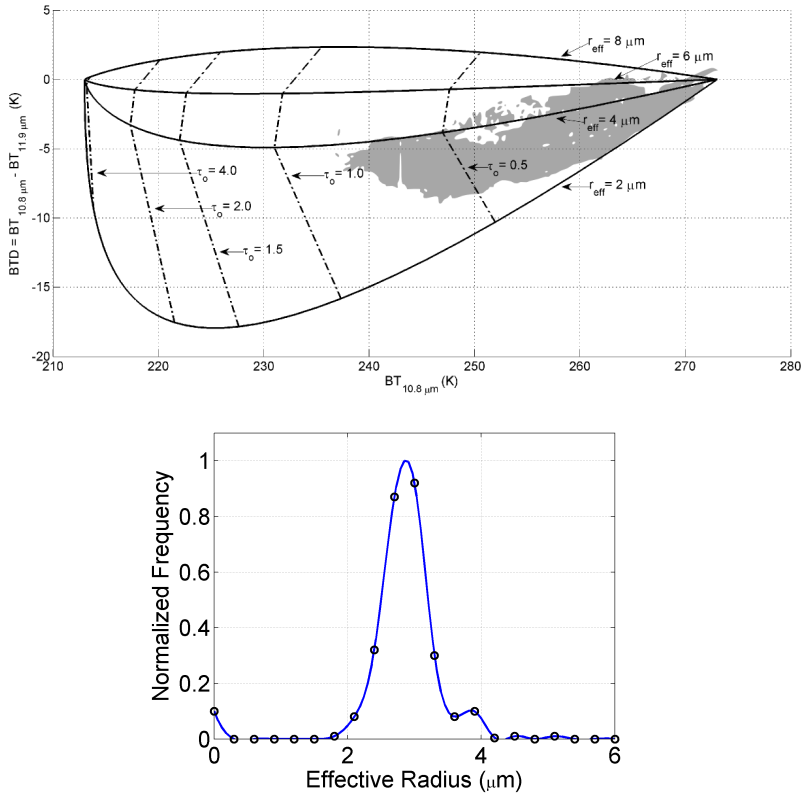

Figure 2.6: Observed Volcanic Temperature Pairs (Top) of Effective Particle Radius Frequency Distribution (Bottom) [10]

Note that particles with an effective radius greater than approximately 5.0 μm will have a positive BTD and are usually discarded because the cloud can not be distinguished from a moisture cloud. It must be stressed that the above frequency distribution of the effective particle radius does not indicate anything about the physical partial size distribution $n(r)$.

2.5.2 Expected Properties of Volcanic Ash Clouds

A typical volcanic ash plume is shown below in Figure 2.7. Note the maximum height of the volcanic ash cloud will be around 15 km with a thickness of 1-3 km [12].

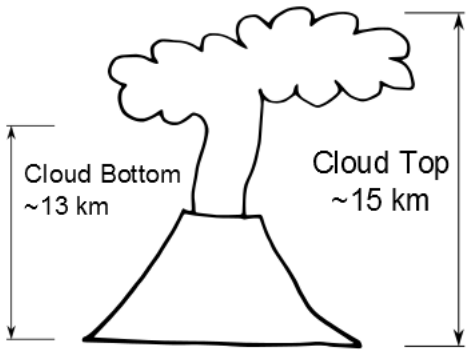

Figure 2.7: Physical Structure of Volcanic Ash Clouds

A compilation of expected parameters for calculating the transmitted radiance through an ash cloud using Equations (2.3) is shown below in Table 2.2 and should be accurate within an order of magnitude. These values are based on data presented by Wen and Rose [10] and assume a log-normal particle distribution, not the uniform particle distribution used earlier.

Table 2.2: Expected Parameters Used to Calculate Transmission of Surface Radiance

Parameter	**Symbol**	**Expected Value**
Extinction Efficency	$Q_{ext,(10.8\mu\text{m})}$	1.8
	$Q_{ext,(11.9\mu\text{m})}$	1.4
Ash Cloud Depth	Δs	2 km
Particle Density	N	6.5×10^6 particles/m^3
Effective Radius	r_e	3.0 μm
Optical Depth	$\tau_{(10.8\mu\text{m})}$	0.662
(Calculated)	$\tau_{(11.9\mu\text{m})}$	0.514

2.6 Calculating Mass Loading

The method of calculating the mass loading, the total mass of the volcanic ash cloud observed by a pixel per unit area, is the subject of Appendix B. First the effective radius of the particles and optical depth of the cloud are found. Then the mass loading is calculated from these parameters using Equation (2.8) shown as

$$u = \frac{2\rho_v \cdot r_{eff} \cdot \tau_o}{3}. \tag{2.8}$$

The effective radius r_{eff} and nominal optical depth τ_o are limited by the BTD method to be

$$1.0\,\mu\text{m} \leq r_{eff} \leq 5.0\,\mu\text{m} \tag{2.9}$$

and

$$0.2 \leq \tau_o \leq 3.0. \tag{2.10}$$

Using the above parameters the limits of the mass loading u and the cloud mass density ρ_c can be calculated. This assumes a cloud thickness of 1 km and a particle mass density of 2.6 g/cm^3 for solid pumice [10] and gives

$$0.35\ \text{g/m}^2 \leq u \leq 26\ \text{g/m}^2 \tag{2.11}$$

and

$$0.00035\ \text{g/m}^3 \leq \rho_c \leq 0.026\ \text{g/m}^3. \tag{2.12}$$

The Civil Aviation Authority of the UK [13] recommends a maximum mass density of 2 mg/m^3 for aircraft traveling through volcanic ash. This is within the detectable range of mass density shown above. A graphical representation of the critical mass loading is given below in Figure 2.8 with a safe level of volcanic ash lying to the right hand side of this curve.

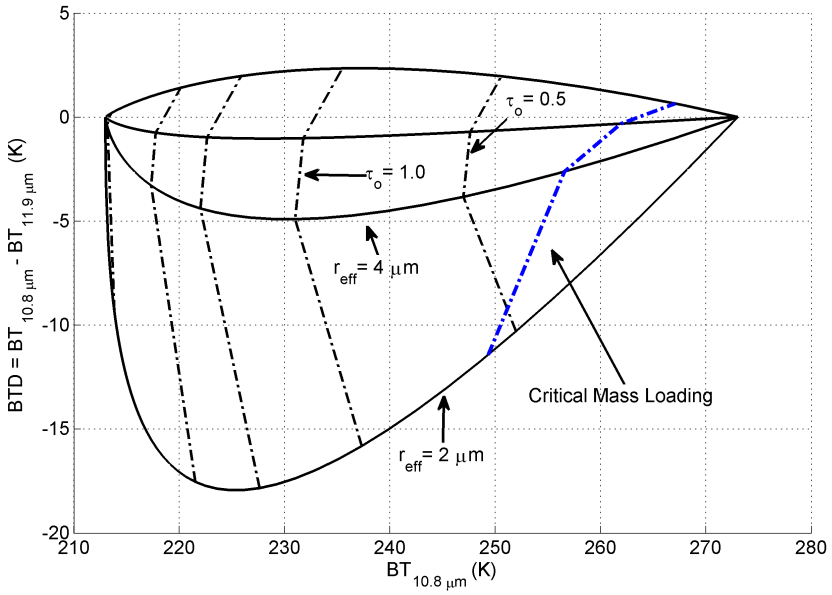

Figure 2.8: BTD Curve with Critical Mass Loading

Therefore the measured brightness temperature at the 11 μm and 12 μm channels can be plotted on the curve above to determine whether estimated cloud mass density is within allowable limits. Any pixel with a BT and BTD that will plot on the left of this critical mass curve will indicate a dangerous level of volcanic ash. A pixel plotted on the right of this curve will indicate a mass density within safety regulations.

2.7 Conclusions

Volcanic ash mass loading can be measured by observing the difference in transmission between the 11 and 12 μm channels. An in-depth analysis requires considering scattering and absorption of particles using Mie theory. The observed radiance is then the transmitted radiance from the earth and the radiated radiance from the cloud. This theory only works for ash particles less than 4-5 μm, however particles of larger radius do not remain air borne as long as the small particles and are typically neglected. The safety of aircraft traffic can be determined by plotting the measured brightness temperatures on a brightness temperature difference chart with the critical mass loading indicated.

Chapter 3
Thermal Sensitivity of Bolometer Sensors

3.1 Scope

This chapter discusses bolometer sensors in terms of how they detect temperature from a distance, the sources of noise that impact these sensors, and how these sources of noise will impact the measurement of temperature from space. The methods of oversampling and image filtering will be discussed for reducing the noise of the sensor.

3.2 Review of Thermal Sensors

Thermal sensors can be broken down into three basic types including photon detectors, coherent receivers, and thermal detectors. The advantages and disadvantages of each sensor type is discussed below.

3.2.1 Photon Detectors

Detectors that have an output signal that corresponds to individual photons incident on the detector are considered photon devices. These consist of a semiconductor material doped to have a certain band-gap energy. Any photon with enough energy to overcome this band-gap energy will temporarily excite the semiconductor by raising an electron to an excited state. This energy relationship is shown below with h being Planck's constant and f being the frequency of the photon. One example is the photo-conductor, which, when exposed to light, will decrease in resistance due to the large number of excited electrons, thereby allowing current to flow easily when a voltage potential is applied. This is represented as

$$E_{photon} = \begin{array}{ll} hf > E_{band-gap} \Rightarrow & \text{Electron is excited} \\ hf < E_{band-gap} \Rightarrow & \text{Electron is not excited} \end{array} . \tag{3.1}$$

The main problem with photon detectors in IR frequencies is that few materials have a band gap energy low enough to be overcome by these low energy photons. Photon detectors that have a sufficiently low band-gap energy must be cooled to cryogenic temperatures. These bulky cooling devices can make implementing an IR camera in a small spacecraft or UAV unfeasible.

3.2.2 Coherent Detectors

Detection of incoming radiation where the phase of the incoming light is measured defines the technique known as coherent detection. This is used for very low frequency IR radiation and uses detection techniques similar to millimeter and microwave technologies. For the 8 to 12 μm range this technique is rarely used and will not be discussed further.

3.2.3 Thermal Detectors

Detectors that absorb all incoming radiation and convert it to heat are considered thermal detectors. Bolometers are the classic example of these detectors. When a bolometer is exposed to incident radiation the sensor has a slight increase in temperature which is proportional to the incoming radiance. If this change in temperature is measured using a thermometer, such as measuring the change of resistance of a thermistor, the change in temperature can be converted to an electrical signal. A simple bolometer detector is shown below in Figure 3.1. Note that the electrical leads perform two roles, the first role being the carrier of electrical current. In addition, these leads will conduct thermal energy and will decrease the sensitivity of the sensor by reducing the change of temperature of the sensor when exposed to radiation. The heat sink will generally be held at some temperature to provide the maximum sensor gain. In the case of a resistor type bolometer, this temperature for maximum sensor sensitivity will correspond to the maximum change in relative resistance with respect to temperature.

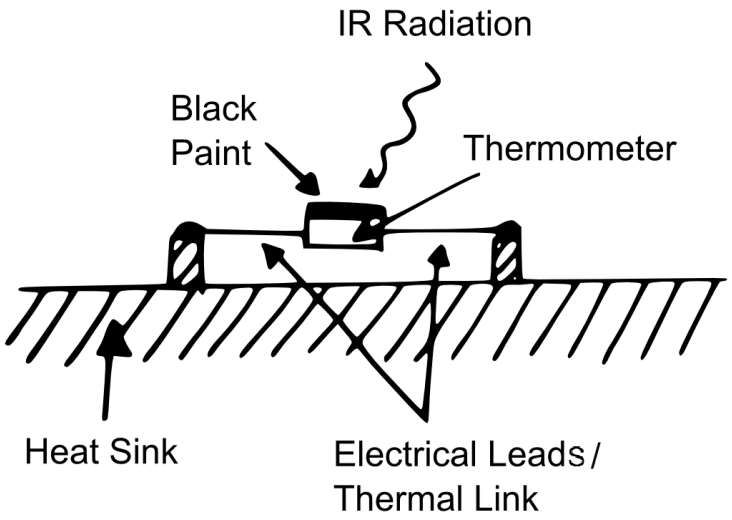

Figure 3.1: Simple Bolometer with Electrical Connection and Thermal Link

3.2.4 Microbolometer Sensor Arrays

Microbolometers are a type of bolometer that are specifically designed to operate at temperatures much larger than crynogenic temperatures. The most common material used for these sensors is Vandium Oxide (VOx) and is designed to have a maximum relative change in resistance with respect to temperature when operated at room temperature. This will then correspond to a maximum sensor response when the sensor is operated at room temperature. These types of sensors allow for very large resolution sensor arrays, such as 640x512 pixels, or even larger. This is the type of sensor that will be considered for radiation detection at 11 to 12 μm in the UAV or small satellites.

3.3 Sources of Noise in Bolometers

There are three main sources of noise for bolometer sensors. This includes the Johnson noise, the thermal link noise, and the photon noise. Each will be discussed briefly.

3.3.1 Referencing of Noise to Absorbed Power

The bolometer is a transducer that converts the temperature of the sensor into an electrical signal. Specifically, the output voltage $V_o(t)$ of the sensor at time t will

be proportional to the total power $P_{abs}(t)$ absorbed by the sensor. This absorbed power will include the IR radiation incident on the detector P_{rad} as well as the $I^2R = P_{bias}$ heating due to a biasing current through the resistor. The radiant responsivity $S_R(T)$ with units of [V/W] is proportional to the relative change of resistance with respect to temperature $\alpha(T)$, also known as the temperature coefficient of resistance. The radiant responsivity relates the output voltage to the absorbed power as shown below in Equation (3.2). Note that the time constant related to the heat capacity of the thermometer is neglected to give

$$V_o(t) = S_R(T) \cdot P_{abs}(t) = S_R(T) \cdot [P_{rad}(t) + P_{bias}]. \tag{3.2}$$

The radiant responsivity $S_R(T)$ is written below as

$$S_R(T) = \frac{\sqrt{R(T)P_{bias}}\eta\{\alpha(T)\}}{G}. \tag{3.3}$$

This chapter will assume that the noise equivalent power density *NEP* will refer to the thermal side of the above equation, with the noise power adding to the absorbed power of the detector and not the signal power of the output voltage. This implies that the fluctuations of the noise voltage at the output can be written as follows, with B representing the noise bandwidth to give

$$\left\langle V_N^2 \right\rangle = S_R(T)^2 \cdot B \cdot NEP^2. \tag{3.4}$$

3.3.2 Johnson Noise

Johnson noise is the circuit noise due to thermal excitation of a resistor. This can be thought of as one-dimensional black body radiation of the resistor but transmitted across wires and transmission lines instead of free space. The noise equivalent power due to Johnson noise, NEP_J, can be calculated as shown below [14]. This includes the noise voltage V_N, the radiant responsivity S_R, the electrical bandwidth B, Boltzmann's constant k, the resistor temperature T, the power dissipated by the resistor due to a biasing current P_{bias}, the thermal conductance of the electrical leads G, the quantum efficiency of the detector η, and the temperature coefficient of electrical resistance $\alpha(T) = \frac{1}{R}\frac{dR}{dT}$ to give

$$NEP_J = \frac{\langle V_N^2 \rangle^{1/2}}{S_R B^{1/2}} = \frac{(4kTR(T)B)^{1/2}}{S_R(T)B^{1/2}} = \left(\frac{(4kT)}{P_{bias}}\right)^{1/2} \frac{G}{\eta\{\alpha(T)\}}. \tag{3.5}$$

Rieke [14] shows that the NEP_J can be approximated for low temperatures as

$$NEP_J \propto GT^{3/2} \text{ for } \alpha(T) \propto T^{-1}. \tag{3.6}$$

This would suggest that a minimal temperature T and thermal conductivity G would generate the smallest amount of thermal noise. However, $\alpha(T)$ will also reduce Johnson noise and therefore microbolometers may have optimal Johnson noise at room temperature where $\alpha(T)$ is maximized for maximum radiant responsivity.

3.3.3 Thermal Link Noise

There will also be noise due to the fluctuations of entropy across the thermal link that connects the bolometer to the heat sink. Rieke gives the noise equivalent power of the thermal link, NEP_T, as follows with G being the thermal conductivity of the electrical leads [14] to give

$$NEP_T = \frac{(4kT^2G)^{1/2}}{\eta}. \tag{3.7}$$

3.3.4 Photon Noise

The fundamental limitation of all bolometer sensors is the photon noise. This is the fluctuations of the number of photons that are absorbed by the detector in any given instant. The electrical analogue is shot noise due to the finite nature of charges passing a boundary. This is simply a consequence of the particlulate nature of photons and can not be reduced by any design choices of the sensor. However, this source is very small when compared to Johnson noise at room temperature and can be ignored. For reference, Rieke gives the noise equivalent power of the photon fluctuations, NEP_{ph}, as follows. Note that ϕ is the number of photons falling on the detector per second [14] and gives

$$NEP_{ph} = \frac{hc}{\lambda}\left(\frac{2\phi}{\eta}\right)^{1/2}. \tag{3.8}$$

3.3.5 Total Noise Power

Because each noise source is incoherent, the total noise equivalent power NEP can be calculated as

$$NEP = \sqrt{NEP_J^2 + NEP_T^2 + NEP_{ph}^2}. \tag{3.9}$$

Once the total NEP is found, Equation (3.4) can be used to find the total noise at the output of the sensor. For bolometers operating at room temperature the noise will be dominated by Johnson noise. However, $R(T)$ will have a strong dependence on temperature and $\langle V_N^2 \rangle$ will not be proportional to temperature as is usually assumed. Therefore, the sensor noise will vary greatly with the temperature of the sensor.

3.4 Uncertainties of Temperature Measurements

As noted earlier, the voltage of the bolometer detector is proportional to the incident radiance. This incident radiance is proportional to the observed body temperature to the fourth power. This is clearly a non-linear relationship between the output voltage of the detector and the equivalent observed temperature. Therefore the actual uncertainty of the observed temperature is not linear in nature. The calculated temperature T with error ΔT is approximately related to the measured radiance J with error ΔJ as shown below. Note that it is assumed that the sensor can detect radiation at all wavelengths by using

$$T + \Delta T = \left[\frac{J + \Delta J}{\sigma}\right]^{1/4}. \tag{3.10}$$

By taking the Taylor series expansion of Equation (3.10) as a function of ΔT the

temperature error can be approximated as shown below in Equation (3.11) and Equation (3.12) to give

$$\Delta T(\Delta J) = \left[\frac{J+\Delta J}{\sigma}\right]^{1/4} - T = \cancel{\left(\frac{J}{\sigma}\right)^{1/4}}^{T} + 1/4\left(\frac{1}{\sigma J^3}\right)^{1/4}\Delta J + \ldots - T \tag{3.11}$$

and

$$\Delta T \approx 1/4\left(\frac{1}{\sigma J^3}\right)^{1/4}\Delta J = \frac{T}{4}\frac{\Delta J}{J} = \frac{1}{4\sigma}\frac{\Delta J}{T^3}. \tag{3.12}$$

The above equation implies that the temperature error ΔT will increase as J and T decrease even though ΔJ may remain constant. Comparing the relative uncertainties is more informative as

$$\frac{\Delta T}{T} = \frac{1}{4}\frac{\Delta J}{J}. \tag{3.13}$$

Therefore the relative temperature error will be approximately one quarter of the relative radiance error.

3.5 Implications to IR Thermal Cameras

Some implications of the previous results are summarized below.

3.5.1 Derating NETD due to Temperature

IR Camera manufacturers usually only give the noise equivalent temperature difference (NETD) when indicating the sensitivity of the camera. This NETD is defined as the uncertainty of the temperature due to sensor noise and reported by FLIR to be 50 mK for the Quark. The NETD listed by IR Camera manufacturers must be de-rated for lower temperatures objects using Equation (3.11). These cameras are usually tested with a source at 25 °C and therefor the listed NETD (≈50 mK) is not an accurate measure of temperature error for ash clouds at -40 °C.

3.5.2 Derating NETD due to Spectral Filters

Because the output voltage signal is proportional to the incident radiance, using a spectral filter will increase the temperature uncertainty. If SW represents the unaltered spectral bandwidth and NSW represents the narrow spectral band-width, the temperature uncertainty can be found as

$$\Delta T = 1/4 \left(\frac{SW^3}{\sigma J^3 \cdot NSW^3} \right)^{1/4} \Delta J. \tag{3.14}$$

Note that the very narrow band-width spectral filters suggested for this design make the approximation $J = \sigma T^4$ invalid along with all of the results in Section 3.4, but the above relationship does provide a rough estimate. The ratio of $(SW/NSW)^{3/4} = (6/0.4)^{3/4} = 7.6$ therefore estimates that the NETD will increase from 0.05 K to 0.75 K when the narrow band spectral filters are used.

3.6 Oversampling

The use of oversampling may be required to increase the SNR to acceptable levels ($\approx$10) and therefore reduce the temperature uncertainty.

3.6.1 *SNR* Improvement

The derivation of the signal-to-noise ratio SNR using oversampling is given here. Let any given signal measurement be denoted as V_m, the ideal signal as V_s and the noise in the signal as V_N. Assume that any change from the signal V_s is insignificant. The measured voltage and initial signal to noise ratio SNR_o can be represented as

$$V_m(t) = V_s + V_N(t)$$

and

$$SNR_o = \frac{V_s^2}{\langle V_N^2 \rangle}.$$

If N samples at intervals of Δt are taken the sum of the signals can be represented as

$$\sum_{n=0}^{N-1} V_m(t+\Delta t \cdot n) = NV_s + \sum_{n=0}^{N-1} V_N(t+\Delta t \cdot n).$$

By assuming that the noise frequency period is much smaller than the sampling time Δt the phase of V_N is essentially random. The maximum and minimum of the summed voltage can then be estimated as

$$\sum_{n=0}^{N-1} V_m(t+\Delta t \cdot n) = NV_s \pm \sqrt{N}\sqrt{\frac{1}{N}\sum_{n=0}^{N-1} V_N^2(t+\Delta t \cdot n)} = NV_s \pm \sqrt{N}\langle V_N^2 \rangle^{1/2}.$$

The new signal to noise ratio using oversampling SNR_s is therefore

$$SNR_s = \left(\frac{NV_s}{\sqrt{N}\langle V_N^2 \rangle^{1/2}}\right)^2 = N \cdot SNR_o. \tag{3.15}$$

Therefore using N samples can increase the SNR by a factor of N. However oversampling will not correct for the following types of noise and error.

- Calibration Errors
- Slowly varying noise such as 1/f noise and thermal drift

3.6.2 Appropriate Number of Samples

The thermal camera has a measured RMS thermal noise quantization value of 4.2 at each pixel. The quantification error of digital data give a minimum uncertainty of $\pm$ 0.5. Therefore 64 samples will reduce the thermal noise to the quantification error limit. More samples will not reduce the error further but less samples can be used as needed. Weather balloons will be moving slow and can take as many samples as required. A UAV will be able to control their speed as needed to achieve the required number of samples.

However, the arbitrary motion of small satellites must be taken into account. A CubeSat traveling at 8 km/s with a pixel resolution of 500 m will then have up to

62.5 ms of sampling time available to move one pixel width. The sampling rate of the IR camera is 25 Hz, giving a total sampling time of 40 ms. Therefore each pixel on the IR camera will be able to sample each 500 x 500 m cloud area a single time. The same area can be re-sampled by the next row of pixels that pass over as the satellite continues its orbit. Because there are 640x512 pixel in the Quark camera the 64 sample maximum will easily be reached, assuming the pixel array is rotated correctly.

The above will only be true if the camera does not have to switch filters. If two separate bands are used there can be up to a 0.5 s delay between bands, giving a total time of $2 \times (0.04 + 0.5)$ s = 1.08 s to image with both bands and rotate the filter wheel twice. This gives a maximum number of samples to be $(0.0625\text{ s} \times 512\ )/1.08\text{ s}$ = 29 samples. Therefore the noise level of ± 4.2 can be reduced to $\pm 4.2/\sqrt{29} \approx \pm 0.8$ but can not be reduced to the theoretical minimum of ± 0.5. Reducing the travel time of the filter wheel is critical for increasing the number of samples and therefore reducing the noise level of the sensor.

3.7 Image Filtering

The white noise of each pixel can be significantly reduced by applying an image filter that removes any high frequency spacial variation. One filter commonly used for noise reduction in image processing is the Wiener filter. The effect of applying this filter to an image is shown below in Figure 3.2. The noise of the sensor is shown to decrease significantly except at the edges where the Wiener filtering algorithm fails. Therefore noise reduction can be achieved by simply applying an image filter.

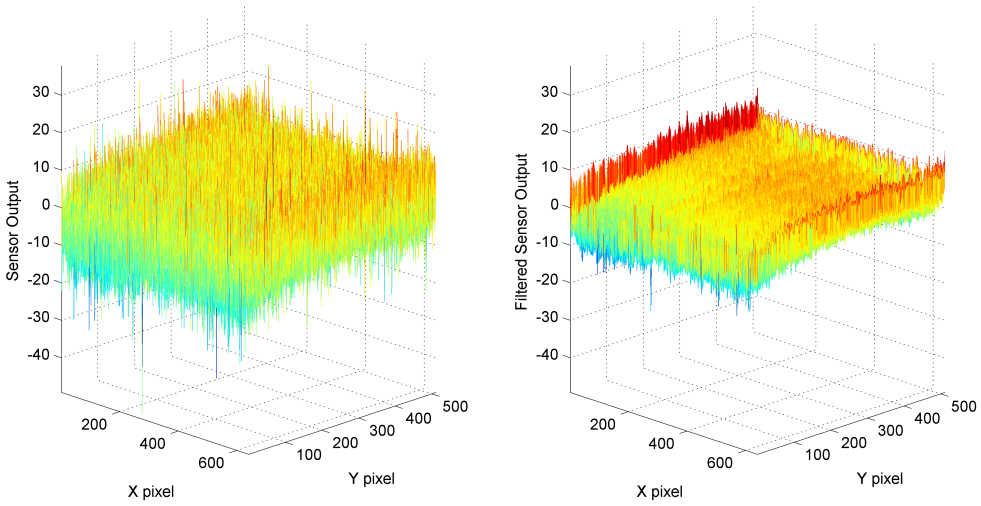

Figure 3.2: Unfiltered (Left) and Filtered (Right) Response of Sensor

The noise using the Wiener filter is measured to be reduced from 4.2 to 1.5 when the boundary of the image is excluded. A similar reduction in noise would require 8 additional image samples. Therefore in order to reduce the sensor noise to within the quantization limit, image filtering over the average of 8 images would be required. This gives a reduced noise of

$$\text{Sensor Noise} \quad = \pm 4.2/\sqrt{(8\text{ filtering}) \times (8\text{ samples})} = \pm 4.2/8 \approx \quad \pm 0.5.$$

The use of image filtering is only valid for smooth functions with slow spacial variations. For example, image filtering would not be useful for accurately measuring the temperature of small hot spots because the sensor response of the hot spot will be partially reduced. This will cause the temperature of the hot spot to be underestimated. However volcanic ash clouds will be diffusive in nature and no rapid spacial changes in concentrations should exist. Therefore, image filtering may be a valid method for reducing the sensor noise level.

3.8 Conclusions

The Quark camera uses a microbolometer sensor that operates at room temperature. Johnson noise is the largest source of noise and measured to have a quantization value of 4.1 on the IR camera. This noise can be reduced to the quantization

limit of 0.5 by averaging over 64 samples. A CubeSat can achieve this high sample rate by measuring each pixel row of the camera as it sweeps over the target, but optimizing the filter wheel travel time is critical to maximizing the number of samples and reducing the sensor noise.

Chapter 4
Design of Thermal Imaging Module

4.1 Scope

This chapter will briefly discuss the optical, mechanical and electronic design of the imaging module. For the purposes of this discussion it is assumed the imaging module will be used primarily for a UAV with the possibility of being converted to a small satellite payload. This material describes the existing design but this design was meant primarily for a lab bench demonstration. More electrical and mechanical design work will be required for a working field unit.

4.2 Optical Components of Imaging System

The thermal imaging system module consists of the following components:

- Quark IR Camera Core
- Band Pass, 10.6 μm and 11.7 μm Spectral Filter
- On-Board Black Body Calibration Source with Thermometer
- Servo Motor for Rotation of Filter Wheel
- Controller for Stepper Motor and Camera
- Raspberry Pi as Embedded Computer for Image Processing

Each of these devices are described below in more detail.

4.2.1 Thermal Camera Selection

The FLIR® Quark camera was chosen because of its extremely small size and reasonable power consumption while giving a large pixel resolution and reasonable sensitivity. This camera is shown below in Figure 4.1 and was purchased for $8200.

Figure 4.1: Quark IR Camera Core by FLIR®

The Quark camera uses a 640x512 pixel microbolometer field pixel array with a pixel pitch of 17 μm. A complete list of specifications is given below [15].

Table 4.1: Quark Specifications

FPA Resolution	640 x 512
Pixel Pitch	17 μm
Spectral Band	7.5 - 13.5 μm
Full Frame Rate	25 Hz
NETD	<50 mK at f/1.0
Scene Range	-40 °C to + 160 °C
Operating Temperature Range	-40 °C to +80 °C

4.2.2 Black Body Source

The black body source (BBS) used for on-board calibration will be mounted on a filter wheel with a temperature sensor attached. An existing filter wheel with a BBS is used in the FireMapper by Space Intruments Inc. and is shown below in Figure 4.2. This BBS will serve two purposes. First it will act like a flat uniform object so the camera can perform its own internal calibration of the sensor, which is called a flat field correction (FFC). Once the FFC is performed, an image of the BBS

will be taken for calibrating the sensor response. A second image will be taken of the BBS at a later time to estimate the thermal drift of the sensor.

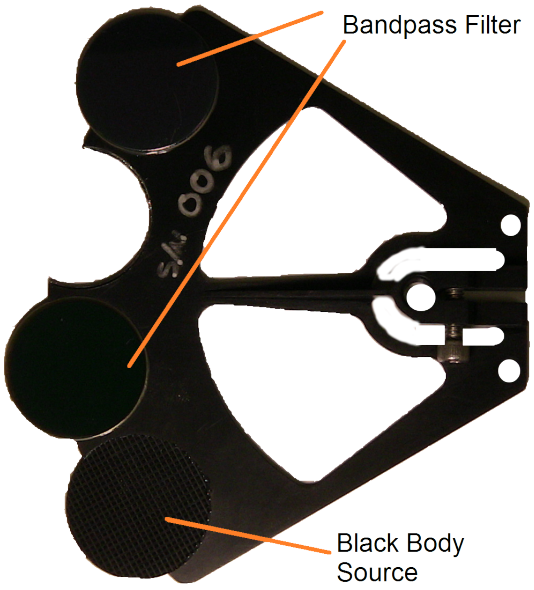

Figure 4.2: Black Body Source in Filter Wheel (Courtesy of Jim Hoffman; Space Instruments, Inc.)

Sensor calibration will also require an accurate temperature measurement of the black body source. Currently a semiconductor based thermometer is used for temperature measurements. This is attached to the back of the BBS.

4.2.3 Spectral Filters

There will be three spectral filters required for this design. One filter required will be an all pass filter, which could be implemented by removing everything in front of the camera. The other two filters are narrow band filters at 10.9 μm and 12.2 μm with a spectral bandwidth of 0.339 μm and 0.506 μm respectively.

4.3 Structural Components

4.3.1 Filter Wheel Design

The filter wheel implementation should follow three main design guidelines:

- Be as light in mass as possible

- Be as small in size as possible
- Be fast enough in rotation speed to allow for sufficient over sampling.

One design that emphasizes the compact requirement was generated by Patrick Wade as shown below in Figure 4.3. One major modification that will be required is to gear the filter wheel optimally to provide the fastest response time from the motor.

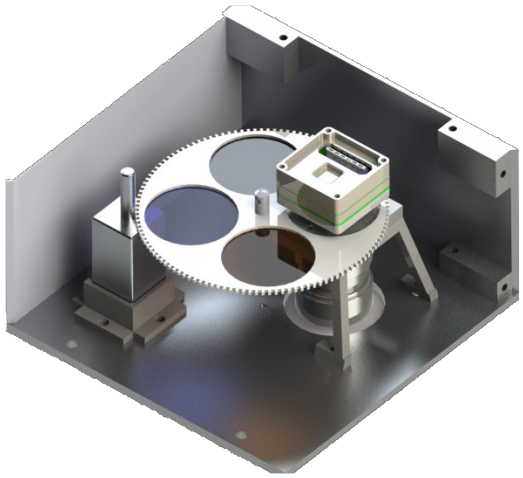

Figure 4.3: Potential Filter Wheel Design

4.3.2 Lab Bench Demonstration

For simplicity a servo motor was used in the lab bench demonstration. The filter wheel and support structure was designed by Kodiak Cullen, Sarah Hoffman, and Aly Wardell of the UAF Mechanical Engineering department and manufactured by Isaac Thompson on his 3D printer. As shown in Figure 4.4 the filter wheel provides housing for two narrow band spectral filters, the on-board black body source and an open slot for the wide-band response.

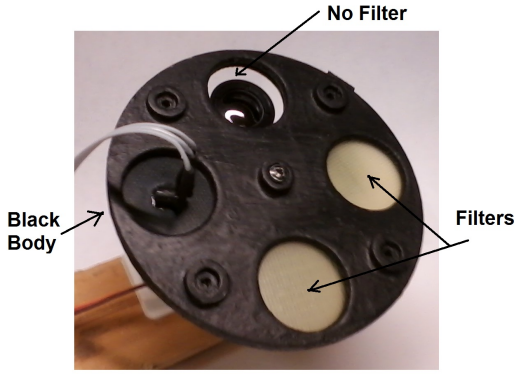

Figure 4.4: Structure

A side view of the physical structure is given in Figure 4.5 and shows the position of the Quark camera and the servo motor for rotation of the filter wheel.

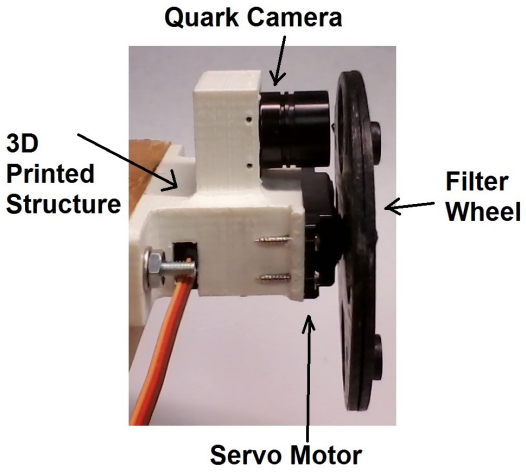

Figure 4.5: Side View of Lab Bench Structure

4.3.3 Further Mechanical Design

Implementing the IR imaging system on a UAV or small aircraft will require significant mechanical design. The most import step will be the mechanical design of the gimbals. These gimbals will provide both image stabilization during a flight as well as allowing for pointing of the IR imaging module. Engineers at the Alaska Center for Unmanned Aircraft Systems Integration (ACUASI) are currently designing gimbals for other applications and can lead this design step.

4.4 Electronic Design

The electronic components include the Raspberry Pi for image processing, a custom designed control board for the servo motor, and a mock UAV for testing the communication interface to the module. All communication from the UAV occurs with the Raspberry Pi which will then communicate to the motor controller and the Quark camera. An overview of the electronic systems is presented below. A more detailed review of the electronic system design is presented in Appendix C.

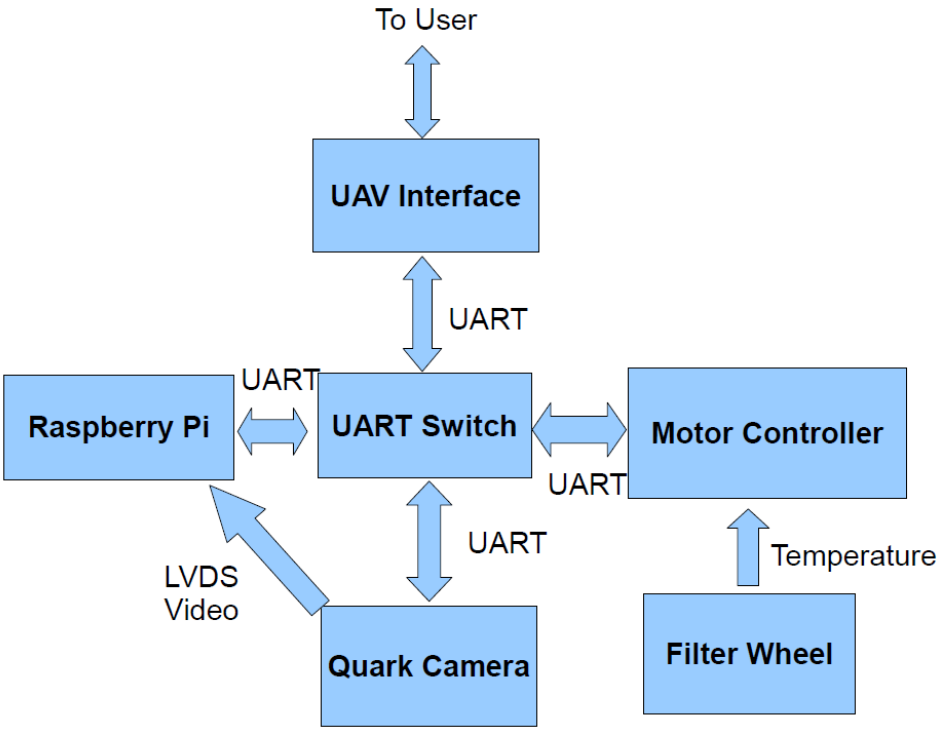

Figure 4.6: Overview of Electronic Systems

4.4.1 Raspberry Pi for Image Processing

The Raspberry Pi was selected as the image processor due to low cost, a large user-base and a preexisting video channel using the LVDS interface. However, this video channel is still being implemented in the design. This processor is shown below in Figure 4.7 with physical dimensions of 85x56 mm, small enough to be suitable for UAV applications.

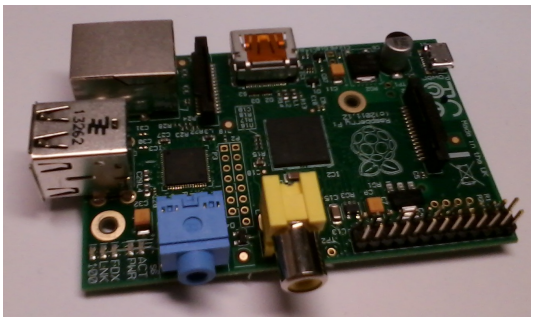

Figure 4.7: Raspberry Pi used as Central Processor

4.4.2 Motor Control Board

A motor control board was developed to deal with the needs of the servo motor. This included adding filtering to prevent ripples on the power supply when the motor is energized. Also, a pulse width modulated signal was sent to the servo motor for position control of the filter wheel. Included on the motor control board was the UART switch between the Raspberry Pi and the other devices. This control board is shown below in Figure 4.8 mounted on top of the Raspberry Pi.

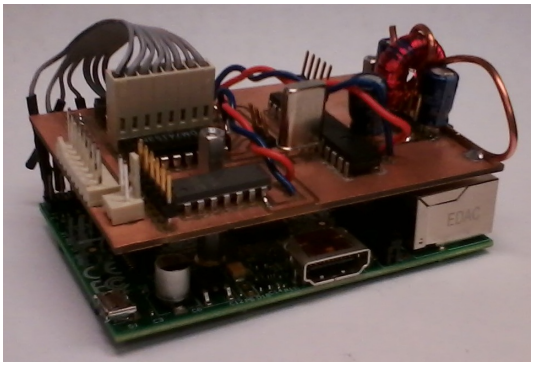

Figure 4.8: Control Board Mounted to Raspberry Pi

This design only used basic capacitor filters and linear voltage regulators for voltage control and stabilization. The power regulation design should be further optimized for a field prototype.

4.4.3 Mock UAV

For laboratory testing of the module, a personal computer connection was required. A mock UAV was designed that would provide power to the module and establish a communication connection with a single connector. This is shown below in Figure 4.9 along with a display screen for viewing the analog output of the camera.

Figure 4.9: Mock UAV for Connecting to a Computer

4.5 Summary

This chapter discussed the design of the thermal imaging module including an overview of the electrical components. Significant mechanical design will be involved in mounting the module to gimbals for camera stabilization and pointing control for field testing of this system from a UAV.

Chapter 5
Testing and Calibration of Imaging System

5.1 Scope

This chapter will describe the techniques for testing and calibrating the IR imaging system. First the testing procedures for characterizing the sensor noise and thermal drift will be discussed. Next the gain of the sensor is measured using a lab bench black body source swept over various temperatures. A calibration technique is presented for correcting the thermal drift of the sensor over a period of up to 1 minute. Variation of the sensor gain with sensor temperature is corrected by testing in the laboratory.

5.2 Corrections Performed by the IR Camera

The Quark camera provides two methods of rough calibration, with the first method being the flat field correction (FFC). An object with a flat response is placed in front of the Quark and a *DO_FFC* command is sent to the camera via the RS-232 communication link. This sets the pixel array with a uniform output, essentially zeroing out any effect of thermal drift. The IR imaging system will use the on-board black body source as the uniform object for performing a FFC. This calibration method is good enough for imaging purposes but not for precise radiometric applications. An additional image of the on-board BBS at a known temperature will be taken and used to relate the sensor output to a known radiance.

The second calibration method used by the Quark is to apply built in calibration tables when the sensor changes temperature. This is because the sensor response of the Quark will depend on the temperature of the sensor pixel array itself. Whenever the pixel array is heated or cooled through 0 °C, 40 °C or 60 °C new internal calibration terms are applied to the sensor output by the Quark. This will help correct for any change in sensor gain when the sensor has large temperature changes. More accurate correction to temperature variation will be achieved by measuring the senor response manually in the laboratory by changing the Quark core temperature in steps of 10 °C and measuring the sensor gain. Note that the sensor should be maintained at room temperature to provide the maximum sensitivity of

the camera.

5.3 Sensor Noise Limit

The Johnson noise of the sensor is measured by first performing a FFC and then recording the sensor response of the camera over time when exposed to the on-board BBS. Note that the Quark does not have an internal shutter and a uniform object, such of the BBS on the filter wheel, must be placed in front of the camera during the FFC. This FFC acts by zeroing out any spacial varaition, leaving only the temporal noise at each pixel. The response immediately after a FFC is shown below in Figure 5.1 with a sensor output standard deviation of 4.2. Therefore the sensor output accuracy is limited to $\approx \pm 4$ and cannot be removed using calibration techniques. Only by taking 64 samples can the noise level be reduced to the quantization limit of ± 0.5.

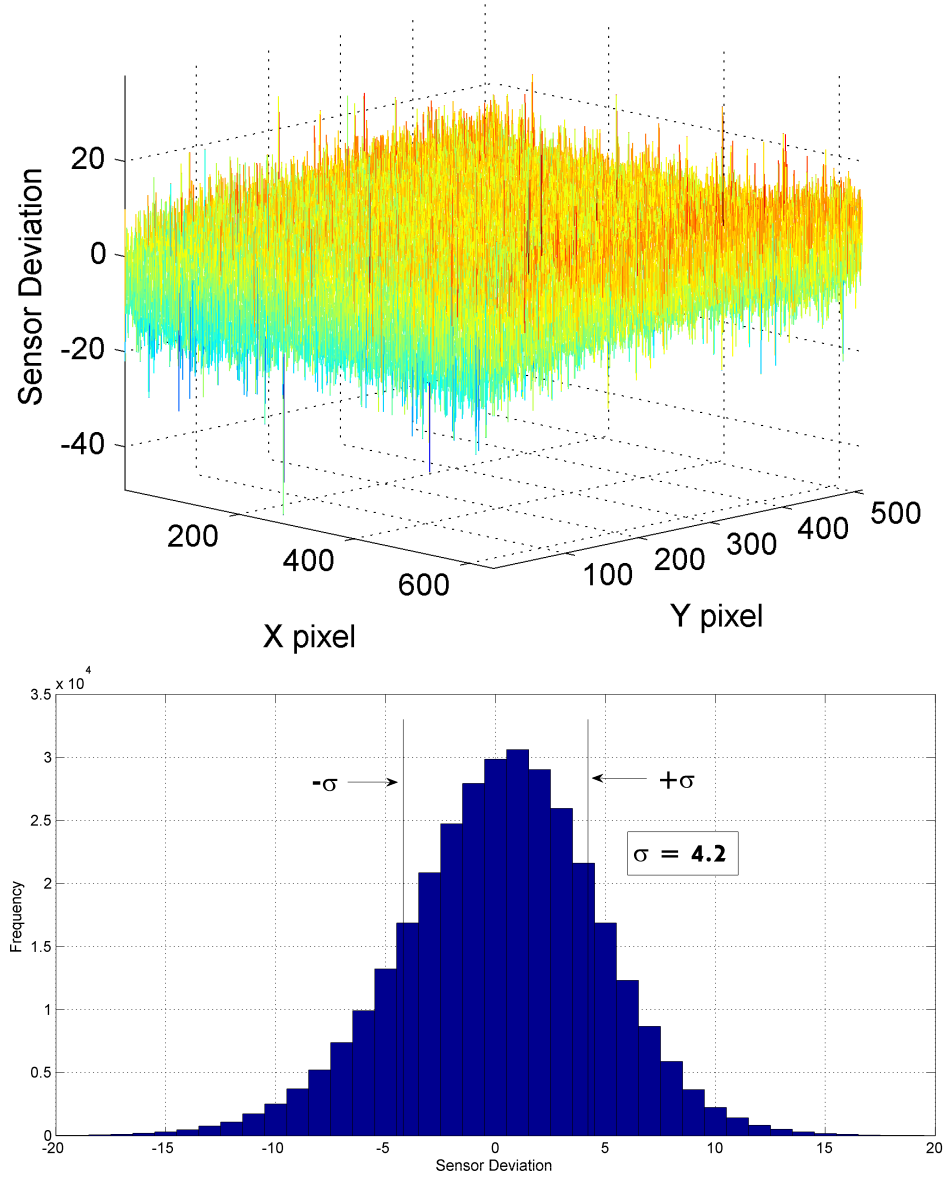

Figure 5.1: Sensor Output Following FFC (Top) and Histogram of Temporal Noise Deviation (Bottom)

5.4 Thermal Drift

The main calibration concern is the drift of the sensor output due to thermal variations of the sensor. A plot of the average sensor output over time is shown below in Figure 5.2 wth samples taken every 45 sec. This shows significant fluctu-

ations of the sensor array with a peak deviation of 80, which is 20 times larger than the Johnson noise. However these fluctuations due to thermal drift are slow. As shown in the bottom plot, the thermal fluctuations can be approximated as linear for periods less than 1 minute.

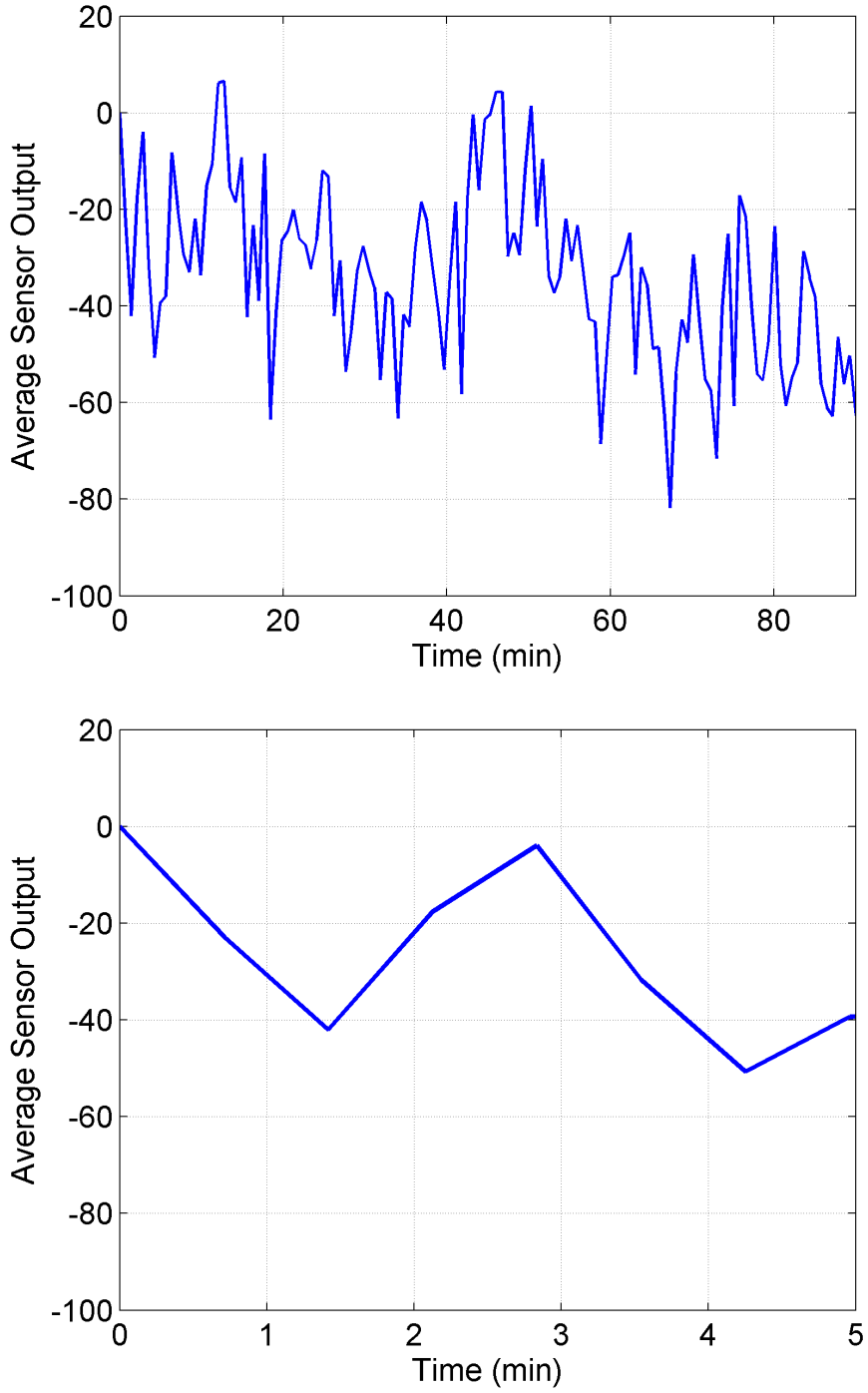

Figure 5.2: Average Sensor Response over 90 min (Top) and 5 min (Bottom)

The power spectrum of the sensor response over 90 min is shown below in Figure 5.3. There is a general 1/f trend present in the data however the Johnson noise

is dominant at frequencies above 10^{-2} Hz. This further suggests that a maximum length of time between calibrations should be less than $1/(10^{-2} \times 2) = 50$ s to limit the effect of 1/f noise.

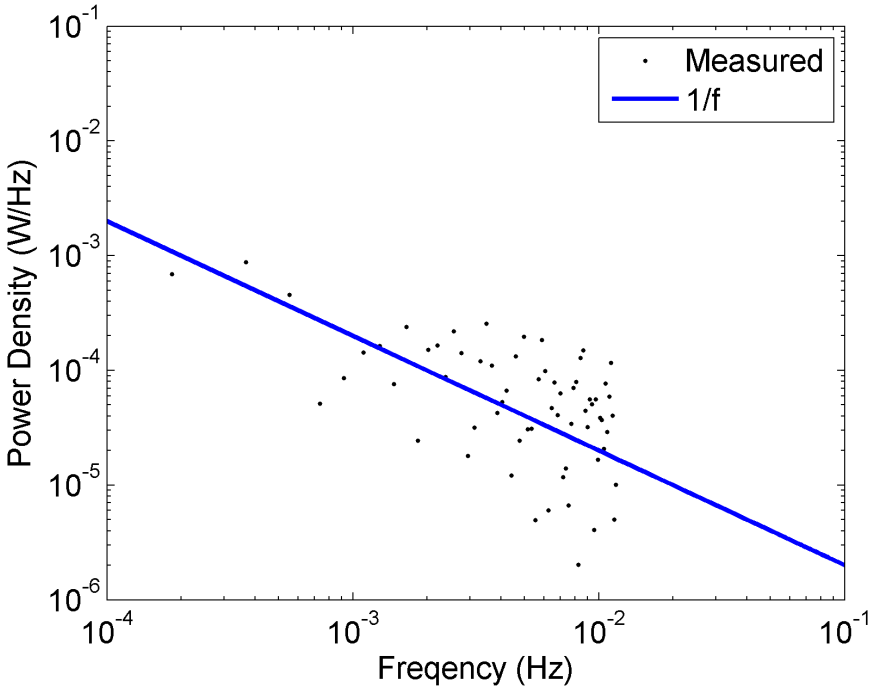

Figure 5.3: Noise Power Spectrum of Sensor

While a 1/f noise spectrum has been shown to exist, the source of this "noise" is actually thermal drift. Removing the thermal drift of the sensor array was found to eliminate this 1/f response shown above but retain the white noise.

5.5 Calibration of Sensor Drift

The linear region of thermal drift is predictable and can be calibrated out. First a FFC is applied to the sensor followed by capturing an image of the on-board black body source as a reference. Several images are taken with the different filters with the capture times recorded for each image. After these images are captured, a final image is taken of the BBS to measure the sensor drift. The previous images are adjusted by adding the linear interpolation of the thermal drift over the period. This is illustrated below in Figure 5.4 with the first captured image giving the zeroed response of the sensor and the final image captured showing the sensor drift over

time.

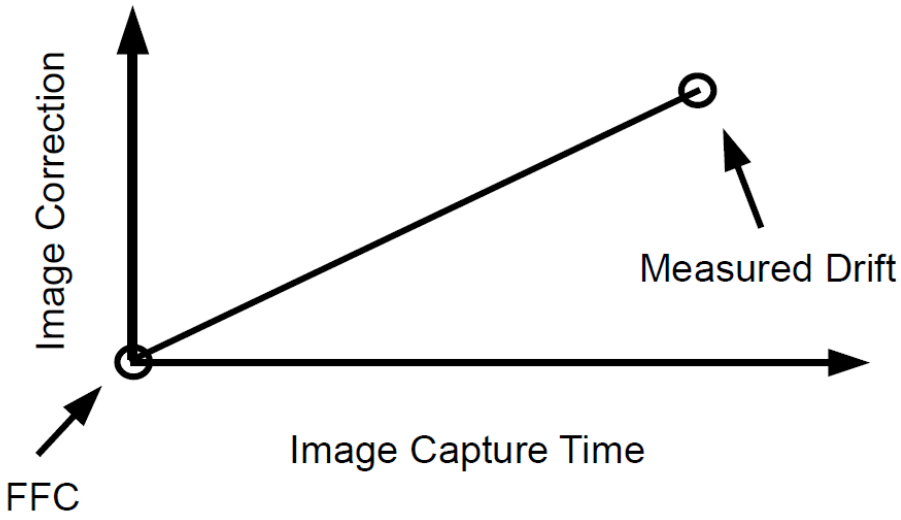

Figure 5.4: Correction of Sensor Drift over Time

5.6 Sensor Gain

In order to convert the sensor output into radiance the sensor gain must be known. This gain term is calculated by sweeping a laboratory black body source across a range of temperatures and comparing the sensor output to the calculated radiance.

5.6.1 Test Setup

The Electro Optical Industries Model ES1000-100/T black body source shown below in Figure 5.5 was used as the reference for accurate response of the sensor array. The IR imager was mounted as shown to calibrate the Quark camera. Temperature of the black body source was swept from 50 °C to 175 °C in steps of 25 °C, with the lower limit due to the BBS and the upper limit due to the camera. Two hours were given to the black body source to stabilize for each temperature setting before taking measurements. Once stabilized a FFC was performed and the response of each filter, including the camera with no filter, was measured.

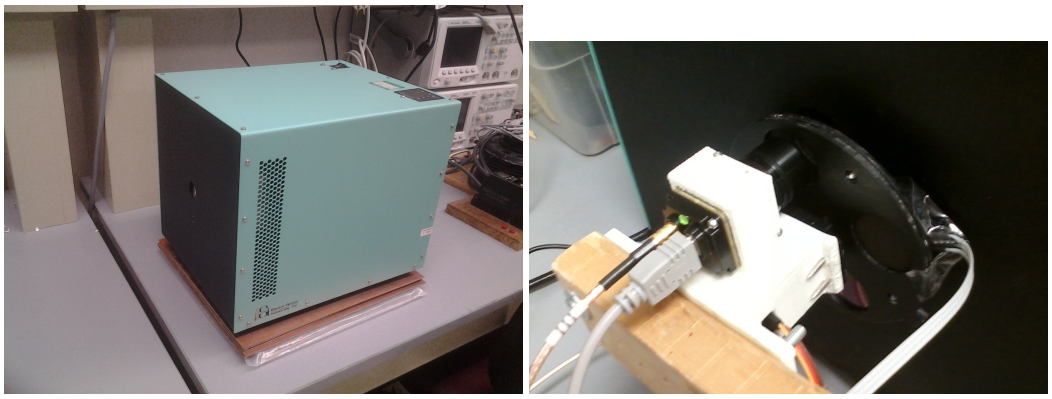

Figure 5.5: Laboratory Black Body Source (Left) and Mounted IR Imaging System (Right)

The resulting image of the lab bench black body source is shown below in Figure 5.6. Note that this is not a uniform image because the black body source has a limited viewing hole. Therefore only pixels near the center of the BBS hole are included in the sensor gain calibration procedure.

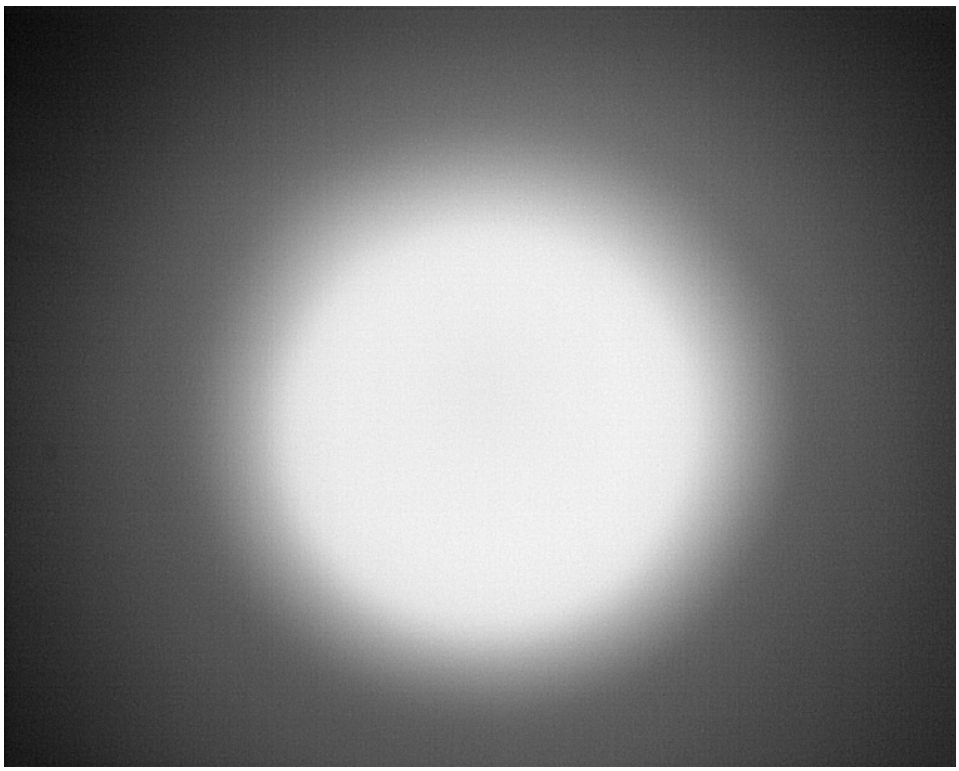

Figure 5.6: Image of Heated Black Body Source

5.6.2 Calculating Spectral Radiance

One required step is to calculate the spectral radiance observed through each filter for a given black body temperature. In the case of the narrow band spectral filters the formula for Planck's black body spectral radiance must be used as shown below in Equation (5.1) with the spectral width $\Delta\lambda$, the spectral transmission of each filter τ_{sf}, and the black body spectral radiance $J_{BB,\lambda}$. This provides the spectral radiance with units of [W m^{-2} sr^{-1} μm^{-1}] as

$$J_{SF,\lambda}(T) = \frac{1}{\Delta\lambda}\int \tau_{sf}(\lambda)J_{BB,\lambda}(\lambda,T)d\lambda. \tag{5.1}$$

In the case of no filter, the Stefan-Boltzmann law must be modified to predict the average spectral radiance. This is shown below in Equation (5.2) to give the appropriate units of [W m^{-2} sr^{-1} μm^{-1}]. Equation (5.1) can also be used with no filter but will give essentially the same result as

$$J_{NF,\lambda}(T) = \frac{\sigma T^4}{\pi\cdot\Delta\lambda}. \tag{5.2}$$

Using the above two equations the spectral radiance of each spectral filter and no filter can be plotted on the same graph for comparison of effective sensor gain.

5.6.3 Measured Sensor Gain

The response of the Quark camera to radiance is presented in Figure 5.7 and gives the linear fit of the sensor response. From this equation it is recognized that the sensor gain (line slope) is 18.883×10^{-3} [W m^{-2} sr^{-1} μm^{-1}]. This sensor gain depends only on the temperature of the sensor array. The offset is found to be -111.871 [W m^{-2} sr^{-1} μm^{-1}] but will change due to thermal drift of the sensor array. Therefore a new offset must be calculated for each measurement to find the actual offset. However, because the maximum sensor drift should nominally be less than 30 over one minute, the offset presented should be accurate to within $\pm30\times18.883\times10^{-3} = \pm0.57$ [W m^{-2} sr^{-1} μm^{-1}].

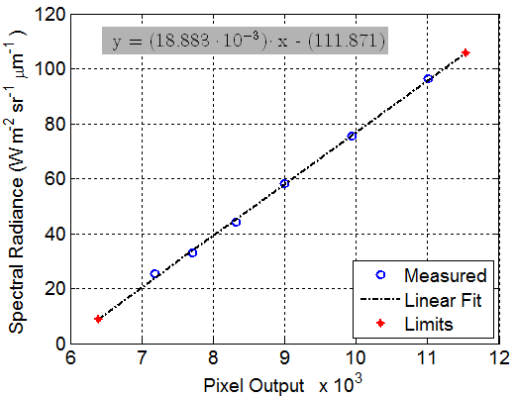

Figure 5.7: Sensor Response of Unfiltered Quark Camera

The spectral radiance compared to the sensor output is shown below in Figure 5.8 including the response of the camera with no filter as well as the narrow band filters. Filters will restrict the radiance exposed to the sensor and will therefore require a larger exposed radiance to have the same sensor output. Note that the measured offset of each spectral response will depend on the temperature of the filter wheel and must be accounted for.

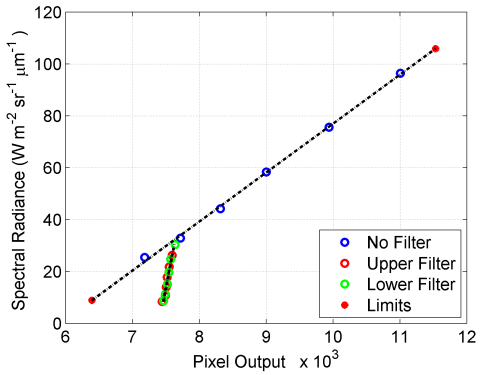

Figure 5.8: Sensor Response of Filtered Quark Camera

The resulting sensor gain and spectral radiance uncertainty ΔJ_λ for each filter is shown below in Table 5.1. A standard sensor noise of 4.2 is assumed to calculate the standard ΔJ_λ while the minimum quantization error of 0.5 is assumed for calculating the minimum ΔJ_λ. This spectral radiance uncertainty will be used for calculating the uncertainty of the mass loading as shown in Appendix B.

Table 5.1: Sensor Gain and Spectral Radiance Uncertainty

Filter	**Sensor Gain** [W/(m sr μm)]	**Standard** ΔJ_λ [W/(m sr μm)]	**Minimum** ΔJ_λ [W/(m sr μm)]
No Filter	18.88×10^{-3}	0.079	0.0094
Upper Band	135.7×10^{-3}	0.569	0.0677
Lower Band	137.7×10^{-3}	0.578	0.0689

5.6.4 Variation of Sensor Gain with Temperature

The sensor will depend on the internal temperature of the sensor array. This temperature can be read by sending the *READ_SENSOR* command over the RS-232 communication channel and is accurate to within 0.1 °C. Using a thermoelectric heat source/sink the temperature of the Quark is swept from below freezing at -11 °C up to 65 °C. The setup used for testing is shown below in Figure 5.9. Ideally the sensor gain variation should be measured across the full operating region of the Quark from -40 °C to 105 °C, but was not due to equipment limitations.

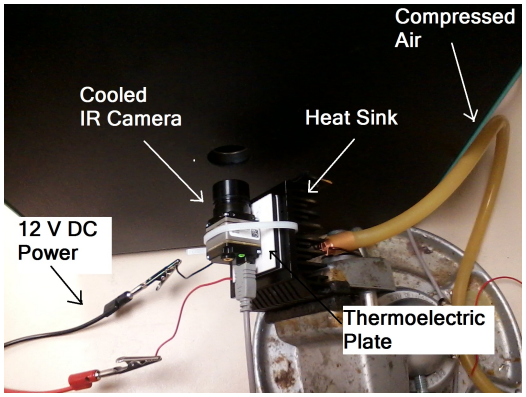

Figure 5.9: Setup for Measuring Variation of Sensor Gain

The sensor gain is found as shown below in Figure 5.10. This sensor gain can vary by a factor of two and therefore cannot be ignored. However, if the internal temperature of the Quark is known the sensor gain can be calculated.

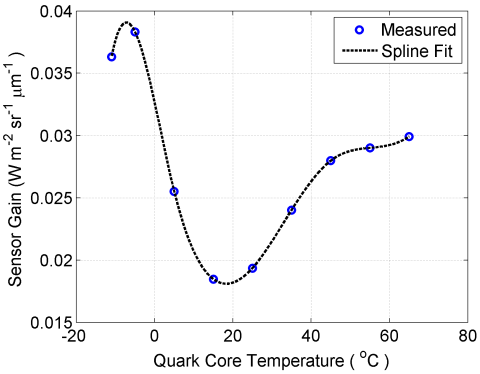

Figure 5.10: Variation of Sensor Gain with Internal Temperature

5.7 Complete Calibration Procedure

The entire calibration procedure consists of five steps shown below in Figure 5.11. First the internal temperature of the Quark is measured which is then used to calculate the sensor gain from Figure 5.10. From here the FFC is performed and an image of the on-board BBS is taken to calculate the sensor offset. The required images are taken and the capture time is recorded. A final image is taken of the BBS a second time in order to find the thermal drift of the sensor over time. From here the raw images taken before are adjusted by assuming a linear sensor drift to provide a more accurate offset.

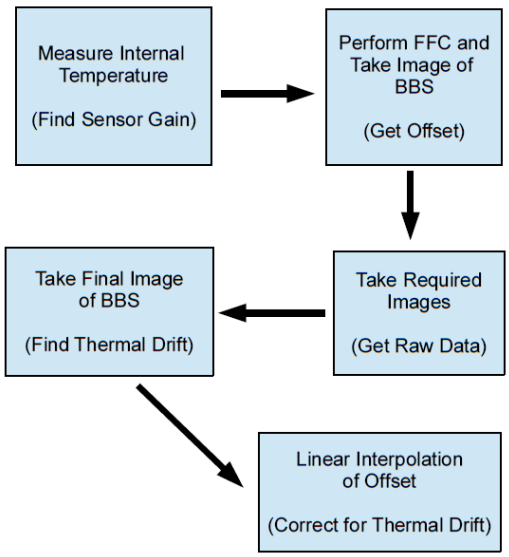

Figure 5.11: Complete Calibration Procedure

The sensor noise can be removed by filtering out the high frequency spacial noise. This will leave a smooth image of the thermal drift. Using this smoothed image will provide a more accurate estimation of the thermal drift by rejecting the effects of white noise.

5.8 Conclusion

The effect of white noise on the sensor was found to be ± 4 and can only be reduced by averaging over multiple samples. Thermal drift was recognized to be much larger in magnitude than the white noise but is slowly varying and can be approximated as a linear variation over one minute or less. The Quark camera response with and without filters was measured and the gain term measured with the Quark held over a range of temperatures, giving a standard sensor noise of 0.57 [W/(m sr μm)]. A complete calibration procedure was presented that calculates the sensor gain from the internal Quark temperature and adjusts for the thermal drift by taking the on-board black body source as a reference to find the sensor offset.

Chapter 6
Electrical Interface with Thermal Camera

6.1 Scope

This section will discuss the basic interface required to control the camera and access the imager data from the sensor using the FLIR® Quark Camera. Most of the information in this chapter comes from the Quark Electrical Interface Description Document (IDD) [16], the Quark Software IDD [17], and the Quark Product Specification [18] as published by FLIR®.

6.2 Connector

Only one connector is require to power, control and interface with the Quark camera. However this requires using a 60-pin Samtec #ST4-30-1.50-L-D-P-TR connector as shown below in Figure 6.1.

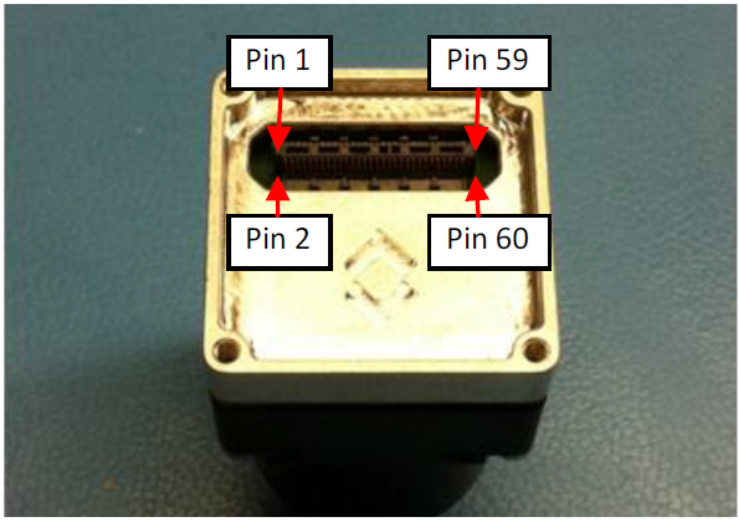

Figure 6.1: Electrical Connection to Quark Camera

The relevant pins used for extracting the data from the camera using the CMOS standard interface is shown below in Table 6.1. Note that the communication ground pin is shared with the power pins DGND. All voltages signals should be 3.3 V.

Table 6.1: Pins Used for CMOS Interface

Pin #	**CMOS Signal (14-bit)**
55	CMOS_CLK
38	CMOS_D0
37	CMOS_D1
40	CMOS_D2
39	CMOS_D3
42	CMOS_D4
41	CMOS_D5
44	CMOS_D6
43	CMOS_D7
46	CMOS_D8
45	CMOS_D9
48	CMOS_D10
47	CMOS_D11
50	CMOS_D12
49	EXT_SYNC
52	CMOS_D13
51	DISCRETE0
54	CMOS_FRAME_VALID
53	DISCRETE_6

The pins used for controlling the camera are shown below in Table 6.2. Note that the RS232 interface voltage is modified to 3.3 V from the standard voltage.

Table 6.2: Pins Used for Camera Control

Pin #	**Communication Pin**
11	SHUTTER1
13	SHUTTER0
15	RS232_RX
16	RS232_TX

The pins used for powering the camera are shown below in Table 6.3. Note that the camera will be fully functional when power is applied. The camera can be shut down by shorting the pin PS_SHDN_N to DGND.

Table 6.3: Pins Used for Power

Pin #	**Power Pin**
9	DGND
10	DGND
17	DGND
18	DGND
21	PS_SHDN_N
35	DGND
36	DGND
57	DGND
58	DGND
59	PWR_IN
60	PWR_IN

6.3 Power Requirements

The electrical power requirements for the camera are summarized below in Table 6.4.

Table 6.4: Power Requirements for Quark Camera

Parameter	**Value**
Input Voltage	3.3 ± 0.1 V
Average Power Dissipation	1.25 W
Average Current Draw	380 mA
Surge Startup Current (for < 8 ms)	< 600 mA

Note that the equivalent capacitance is 2.9 mF to store the energy drawn at the surge current of 600 mA for 8 ms. However the surge current is not much greater than the continuous current so it does not present a large challenge to overcome.

6.4 Camera Control Interface

The camera is controlled using the RS-232 interface using the pins listed in Table 6.2 along with DGND. This is described in detail in the Quark Software IDD. Some useful commands using this interface are presented here. A collection of commands useful for the flat field correction is shown below in Table 6.5.

Table 6.5: Commands Relevant to FFC

ID	Function Code (hex)	Command
11	0x0B	FFC_MODE_ SELECT
12	0x0C	DO_FFC
13	0x0D	FFC_PERIOD
14	0x0E	FFC_TEMP_ DELTA
60	0x3C	FFC_WARN_TIME
121	0x79	SHUTTER_POSITION
198	0xC6	WRITE_NVFFC_TABLE

Another useful set of commands for radiometry is shown below in Table 6.6. Note that while these commands are implemented by the FLIR® Tau cameras, these commands may not be implemented on the Quark so their functionality should be checked before use. The Quark is a relatively new camera and the documentation available is not complete. FLIR® should be contacted directly to verify that the published instructions for interfacing to the Quark is accurate.

Table 6.6: Commands used for Radiometry

ID	Function Code (hex)	Command
10	0x0A	GAIN_MODE
31	0x1F	SPOT_METER_ MODE
34	0x22	ISOTHERM
35	0x23	ISOTHERM_ THRESHOLDS
42	0x2A	GET_SPOT_METER
43	0x2B	SPOT_DISPLAY
67	0x43	GET_SPOT_METER_ DATA
77	0x4D	SHUTTER_TEMP
142	0x8E	TLIN_COMMANDS
219	0xDB	GAIN_SWITCH_ PARAMS
229	0xE5	LENS_RESPONSE_PARAMS

Due to the restricted power and computational capabilities it may be more feasible to take images at selected times instead of processing a live video feed. Some useful commands for requesting a snap shot from the Quark camera are listed below in Table 6.7.

Table 6.7: Commands Used for Snap-Shots

ID	Function Code (hex)	Command
130	0x82	TRANSFER_FRAME
196	0xC4	MEMORY_STATUS
210	0xD2	READ_MEMORY
212	0xD4	ERASE_MEMORY_ BLOCK
213	0xD5	GET_NV_MEMORY_SIZE
214	0xD6	GET_MEMORY_ ADDRESS

An extensive listing of commands available is given in the Tau 2 / Quark Software IDD.

6.5 Shutter Interface

If the Quark detects that the camera has had a significant variation in temperature, it will attempt to perform a flat field correction (FFC) by sending a signal to engage an external shutter. The signal SHUTTER0 will send a signal to close the shutter while the SHUTTER1 will send a signal to open the shutter. These signals will not be used and the FFC will be performed manually by the on-board control processor. Note that the camera must be put in manual mode to prevent the Quark from automatically performing a FFC.

6.6 CMOS Data Interface

The Quark camera can be configured to output data using the CMOS interface and will therefore be equivalent to accessing a standard CMOS camera. Note that the 14-bit CMOS data is required to access the pre-AGC (Automatic Gain Control) signal. The timing diagram for the line acquisition is shown below in Figure 6.2 and published by FLIR® [16].

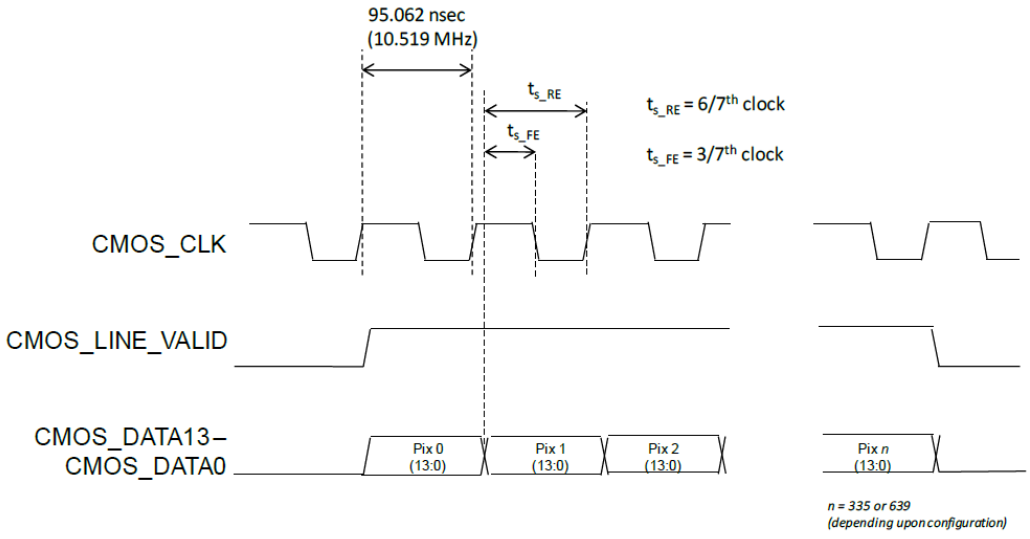

Figure 6.2: Line Timing of the CMOS Protocol [16]

Each frame consists of multiple lines. The timing for a total frame acquisition is shown below in Figure 6.3 and published by FLIR® [16].

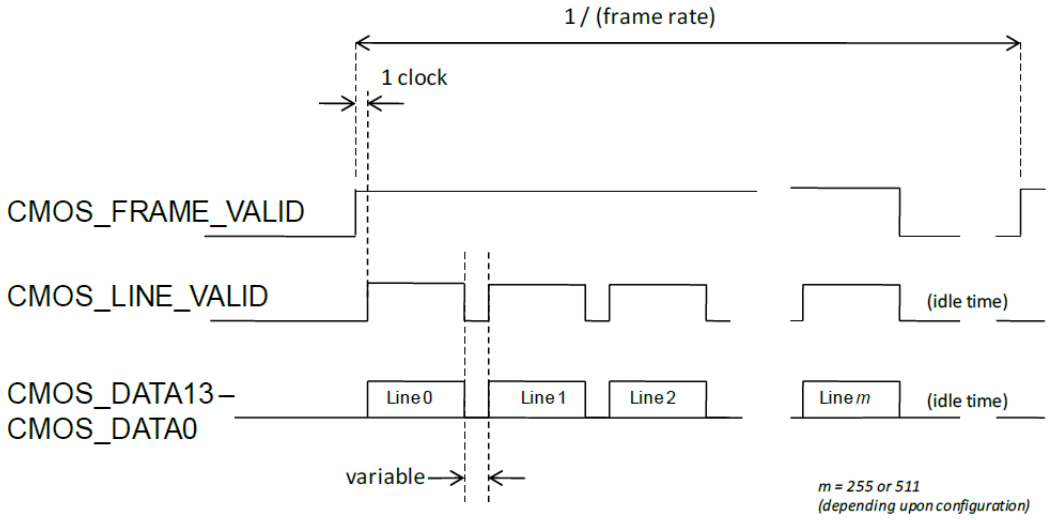

Figure 6.3: Frame Timing of the CMOS Protocol [16]

The above figures can be found in section 3.1.4.2 of the Quark Electrical IDD along with other details of the CMOS interface.

6.7 Interface Prototype

The RS-232 communication interface has successfully been implemented. Commands have successfully sent to and from the Quark and verified, including performing a FFC and capturing a snap shot. The Raspberry Pi is limited in communication speed and has a maximum baud rate of 57.6 kbps. This results in a nearly 10 min wait to capture and entire image by using the RS-232 communication channel.

As of now the high speed digital video channel has not been successfully implemented.

6.8 Overview

The communication interface and video channel of the Quark camera has been discussed. Various commands are available to send to the Quark camera including performance of a FFC and take an image snapshot. While the RS-232 communication channel is operational and communicates with the Raspberry Pi, the high speed video link has not been established to date.

Chapter 7
Conclusions

It has been established that small spacecraft with thermal infrared imaging capabilities may be capable of detecting dangerous levels of volcanic ash that can severely damage jet aircraft engines and must be avoided. Grounding aircraft after a volcanic eruption may cost the airlines millions of dollars per day, while accurate knowledge of volcanic ash density might allow for safely routing aircraft around dangerous levels of volcanic ash. There are currently limited numbers of satellites with TIR imaging capabilities so the elapsed time between revisits can be large, and these instruments can only resolve total mass loading along the line-of-sight. Multiple small satellites could allow for decreased revisit times as well as multiple viewing angles to reveal the three-dimensional structure of the ash cloud through stereoscopic techniques. The design and laboratory evaluation of a TIR imaging system that is designed to fit within the resource constraints of a multi-unit CubeSat to detect volcanic ash mass loading was presented.

The laboratory prototype of this TIR imaging system uses a commercial off-the-shelf (COTS) camera with an uncooled microbolometer sensor, two narrowband filters, a black body source and a custom filter wheel. The infrared imaging system detects the difference in attenuation of volcanic ash at 11 μm and 12 μm by measuring the brightness temperature at each band. The brightness temperature difference method is used to measure the column mass loading. Multi-aspect images and stereoscopic techniques are needed to estimate the mass density from the mass loading.

Laboratory measurements were used to characterize the noise level to be 4.2 and the thermal drift of the sensor to be approximately linear for less than 1 minute. A five step calibration technique was developed to compensate for sensor temperature drift. The detection threshold of volcanic ash density of this TIR imaging system was found to be from 0.35 mg/m^3 to 26 mg/m^3 for ash clouds that have thickness of 1 km, while ash cloud densities greater than 2.0 mg/m^3 are considered dangerous to aircraft. This analysis demonstrates that a TIR imaging system for de-

termining whether the volcanic ash density is dangerous for aircraft is feasible for multi-unit Cubesat platforms.

References

[1] Walsh, B.; Van Dyk, D.; Smith, A. *The Cloud that Closed a Continent. Time.*, Vol. 175(Issue 17.):pg. 24–29., May 2010.

[2] Volcano World. *Cost of Volcanic Eruptions.* [Online]. Available: http://volcano.oregonstate.edu/cost-volcanic-eruptions, June 2014.

[3] NASA. *Landsat 8 Bands.* [Online]. Available: http://landsat.gsfc.nasa.gov/?page_id=5377, June 2013.

[4] NASA. *Advanced Very High Resolution Radiometer - AVHRR*. [Online]. Available: http://noaasis.noaa.gov/NOAASIS/ml/avhrr.html, November 2013.

[5] USGS. *AVHRR Overview.* [Online]. Available: https://lpdaac.usgs.gov/ products/aster_products_table/aster_overview, April 2014.

[6] NASA. *About Modis - Specifications.* [Online]. Available: http://modis.gsfc.nasa.gov/about/specifications.php, June 2014.

[7] Mentch, D. B. *CubeSat Attitude Control Utilizing Low-Power Magnetic Torques & a Magnetometer*. PhD thesis, University of Alaska Fairbanks, 2011.

[8] Prata, A. J. *Observation of volcanic ash clouds in the 10-12 μm window using AVHRR/2 data*. International Journal of Remote Sensing, 10(4 and 5):751–761, 1989.

[9] Petty, G. W. *A First Course in Atmospheric Radiation*. Sundog Publishing, 2006.

[10] Wen, S.; Rose, W. I. *Retrieval of sizes and total masses of particles in volcanic clouds using AVHRR bands 4 and 5.* Journal of Geophysical Research, 99(D3):5421–5431, March 1994.

[11] Prata, A. J. *Infrared Radiative Transfer Calculation for Volcanic Ash Clouds*. Geophysical Research Letters, 16(11):1293–1296, 1989.

[12] Simpson, J. J. ; Hufford, G.; Pieri, D.; Berg, J. *Failures in Detecting Volcanic Ash from a Satellite-Based Technique*. Remote Sensing of Environment, 72(2):191–218, 2000.

[13] CAA, UK. *Guidance regarding Flight Operations in the Vicinity of Volcanic Ash.* [Online]. Available: http://www.caa.co.uk/docs/1425/20110526GuidanceRegardingFlightOperationsInTheVicinityOfVolcanicAsh.pdf, May 2011.

[14] Rieke, G. H. *Detection of Light: From the Ultraviolet to the Submillimeter*. Cambrige University Press, 2003.

[15] FLIR. *Quark Specifications*. [Online]. Available: http://www.flir.com/cvs/cores/view/?id=51266&collectionid=549&col=51275, June 2014.

[16] FLIR. *Quark Electrical Interface Description Document*. [Online]. Available: http://www.flir.com/cvs/cores/view/?id=51266&collectionid=549&col=51276, October 2013.

[17] FLIR. *Quark Software Interface Description Document*. [Online]. Available: http://www.flir.com/cvs/cores/view/?id=51266&collectionid=549&col=51276, October 2013.

[18] FLIR. *Quark Product Specification*. [Online]. Available: http://www.flir.com/cvs/cores/view/?id=51266&collectionid=549&col=51276, October 2013.

[19] van de Hulst, H. C. *Light Scattering by Small Particles*. Dover Publications, Inc., 1981.

Appendix A
Mie Scattering of Dielectric Spheres

A.1 Theoretical Relationships

The scattering and extinction efficiencies are given by van de Hulst [19] for dielectric spheres of index of refraction m. The main results are presented below as

$$Q_{ext} = \frac{2}{x^2}\sum_{n=1}^{\infty}(2n+1)\mathrm{Re}[a_n + b_n] \tag{A.1}$$

and

$$Q_{sca} = \frac{2}{x^2}\sum_{n=1}^{\infty}(2n+1)\left[|a_n|^2 + |b_n|^2\right]. \tag{A.2}$$

From here two parameters are required for the infinite series, a_n and b_n. These are found using the modified spherical Bessel functions $\psi_n(x)$ and $\zeta_n(x)$ as

$$a_n = \frac{\psi_n'(mx)\cdot\psi_n(x) - m\cdot\psi_n(mx)\cdot\psi_n'(x)}{\psi_n'(mx)\cdot\zeta_n(x) - m\cdot\psi_n(mx)\cdot\zeta_n'(x)}, \tag{A.3}$$

$$b_n = \frac{m\cdot\psi_n'(mx)\cdot\psi_n(x) - \psi_n(mx)\cdot\psi_n'(x)}{m\cdot\psi_n'(mx)\cdot\zeta_n(x) - \psi_n(mx)\cdot\zeta_n'(x)}, \tag{A.4}$$

$$\psi_n(z) = zj_n(z) = \sqrt{\frac{\pi z}{2}}J_{n+1/2}(z), \tag{A.5}$$

and

$$\zeta_n(z) = zh_n^{(2)}(z) = \sqrt{\frac{\pi z}{2}}\left[J_{n+1/2}(z) - iY_{n+1/2}(z)\right]. \tag{A.6}$$

For numerical simplicity the derivatives $\psi_n'(x)$ and $\zeta_n'(x)$ can be found using the recurrence relationships of Bessel functions shown below. Note that these relations are also true for $Y_\nu(x)$ and $H_\nu^{(2)}(x)$. These relationships are

$$J_{\nu-1}(x) + J_{\nu+1}(x) = \frac{2\nu}{x}J_\nu(x) \tag{A.7}$$

and

$$J_{\nu-1}(x) - J_{\nu+1}(x) = 2J_\nu'(x). \tag{A.8}$$

This gives the following formulas of the spherical Bessel functions for simple numerical evaluation,

$$\psi_n'(x) = \sqrt{\frac{\pi x}{2}}\left[\frac{n+1}{x}J_{n+1/2}(x) - J_{n+3/2}(x)\right] \tag{A.9}$$

and

$$\zeta_n'(x) = \sqrt{\frac{\pi x}{2}}\left[\frac{n+1}{x}\left(J_{n+1/2}(x) - iY_{n+1/2}(x)\right) - \left(J_{n+3/2}(x) - iY_{n+3/2}(x)\right)\right]. \tag{A.10}$$

These above relationships are used in the MATLAB® function *Q_ideal.m* that is used for evaluation of the extinction and scattering coefficients. Note that the inputs are the size factor $x = \frac{2\pi \cdot r_{eff}}{\lambda}$, the complex index of refraction m and the number of terms to include in the series.

A.2 Verification of Numerical Method

The numerical method in *Q_ideal.m* was verified for an index of refraction of 1.33, corresponding to a spherical water droplet in the visible spectrum. A comparison of the calculated extinction efficiency compared to the size factor is shown below in Figure A.1. This matches the plot given by Petty [9]. Therefore the function *Q_ideal.m* can be assumed accurate as far as the model of an ideal dielectric sphere is accurate. Other more accurate scattering models will not be discussed further but can be found in the literature.

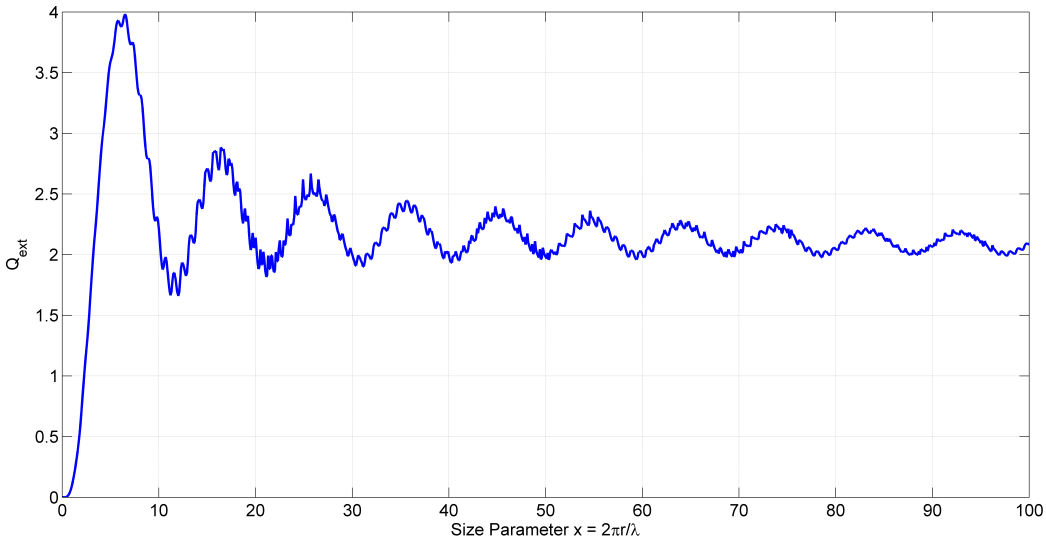

Figure A.1: Calculated Extinction Efficiency for Index of Refraction of 1.33

Appendix B
Estimating Value and Error of Mass Loading

B.1 Introduction

This section discusses the sources of error to the estimation of the mass loading of the volcanic ash cloud. The overall uncertainty is important for deciding whether this imaging system is feasible for volcanic ash cloud mass loading measurements. A graphical and analytic method for calculating the mass loading of volcanic ash is presented. Note that each method first finds the effective radius of the particles and then calculates the mass loading.

B.2 Graphical Estimation of the Mass Loading

The mass loading can be calculated from the mass density of the volcanic material ρ_v, the effective radius of particles r_{eff} and the nominal optical depth τ_o using Equation (B.1). Therefore r_{eff} and τ_o must be found to calculate the mass loading as

$$u \equiv \left(\frac{\text{mass}}{\text{particle}}\right)\left(\frac{\text{\# particles}}{\text{area}}\right) = (\rho_v \frac{4\pi}{3} r_{eff}^3)(\Delta l \cdot n),$$

$$\tau_o \equiv \left(\frac{\text{cross section area}}{\text{particle}}\right)\left(\frac{\text{\# particles}}{\text{area}}\right) = (A)\cdot(\Delta l \cdot n) = \left(2\pi r_{eff}^2\right)\left(\frac{u}{\rho_v \frac{4\pi}{3} r_{eff}^3}\right) = \frac{3u}{2\rho_v r_{eff}},$$

and therefore

$$u = \frac{2\rho_v \cdot r_{eff} \cdot \tau_o}{3}. \tag{B.1}$$

Both parameters r_{eff} and τ_o can now be found from Figure B.1. Then the mass loading can be calculated directly.

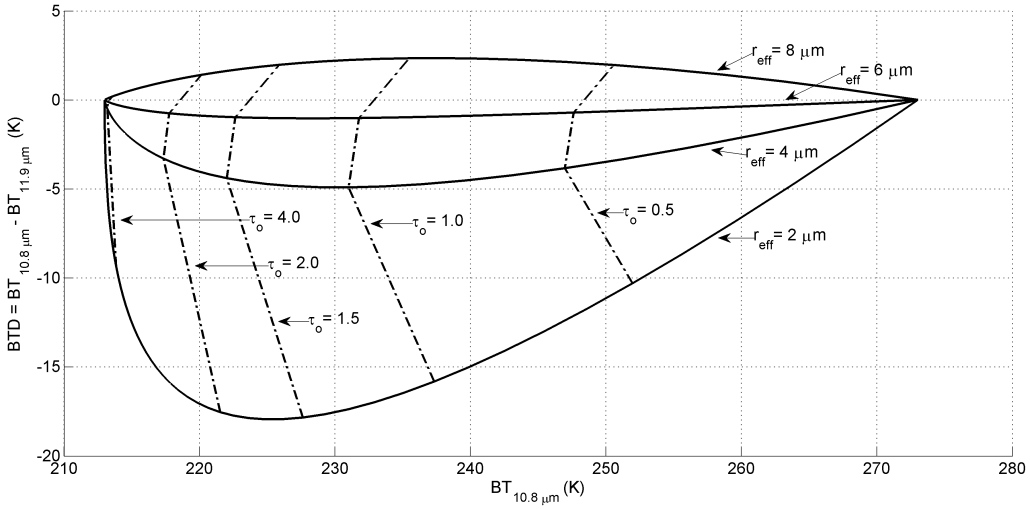

Figure B.1: BTD Chart for Extracting r_{eff} and τ_o

B.3 Analytic Calculation of the Mass Loading

This section will assume that scattering can be ignored. The scattering coefficient Q_{sca} is then assumed to be zero which then implies that $Q_{ext} = Q_{abs}$. This section will also assume that the particle size distribution is uniform, so that all particles have the same physical radius.

The first step is to start with the received radiance of the sensor

$$J_{rec}(\lambda) = \varepsilon_g BB_\lambda(T_g,\lambda)e^{-\tau_o \overbrace{Q_{ext}}^{Q_{abs}+Q_{sca}}(r_{eff},\lambda)} + BB_\lambda(T_c,\lambda)\cdot(1-e^{-\tau_o Q_{abs}(r_{eff},\lambda)}). \tag{B.2}$$

By solving Equation (B.2) for the nominal optical depth τ_o the following expression is found. Note that R_λ is a ratio of radiance and depends on wavelength as well as the measured radiance to give

$$\tau_o = \frac{1}{Q_{abs}(r_{eff},\lambda)} \ln\left[\frac{\varepsilon_g e^{-\tau_o \overbrace{Q_{sca}}^{0}} BB_\lambda(T_g,\lambda) - BB_\lambda(T_c,\lambda)}{J_{rec}(\lambda) - BB_\lambda(T_c,\lambda)}\right] = \frac{1}{Q_{abs}(r_{eff},\lambda)} \ln[R_\lambda]. \tag{B.3}$$

Note that the nominal optical depth τ_o does not depend on wavelength and is constant for both measurements. However τ_o depends on the effective radius r_{eff}.

Therefore a new term is introduced, called the absorption gain term G_{abs} and is defined as

$$G_{abs}(r_{eff}) = \frac{Q_{abs,\lambda_u}(r_{eff})}{Q_{abs,\lambda_l}(r_{eff})}. \tag{B.4}$$

This is plotted as shown below in Figure B.2. Note that this function is not monotonously increasing so the inverse function G_{abs}^{-1} is not singled valued and must be modified so it is single valued. A quadratic fit was chosen and clearly has a monotonic response over the acceptable range.

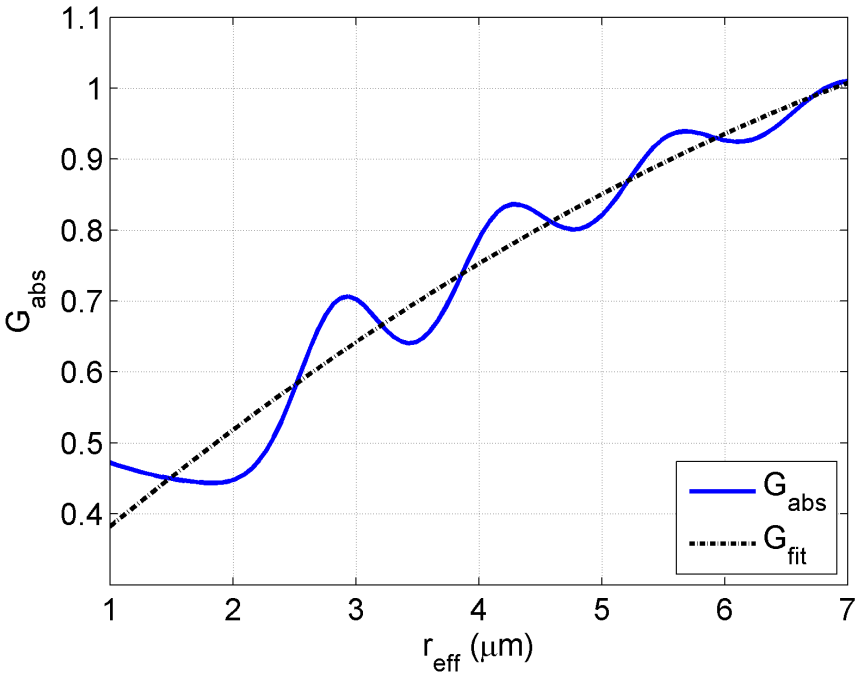

Figure B.2: Absorption Gain Term compared to Particle Radius

Because τ_o is constant, the gain term can be calculated from Equation B.3 as

$$G_{abs} = \frac{Q_{abs,\lambda_u}}{Q_{abs,\lambda_l}} = \frac{\ln[R_{\lambda_u}]}{\ln[R_{\lambda_l}]}. \tag{B.5}$$

By neglecting scattering and setting $Q_{sca} = 0$, the gain term can be calculated using the measured received radiance. This gain term from measured radiance is used to

find the effective radius. The fitted polynomial and inverse function is included as

$$G_{fit} = -0.006422 \cdot (r_{eff}\ [\mu\text{m}\ ])^2 + 0.15564 \cdot (r_{eff}\ [\mu\text{m}\ ]) + 0.2327,$$

$$G_{fit}^{-1}(G_{abs}) = (12.12 - 12.48 \cdot \sqrt{1.176 - G_{abs}})\ [\mu\text{m}\ ],$$

and

$$r_{eff} = G_{fit}^{-1}\left(\frac{\ln[R_{\lambda_l}]}{\ln[R_{\lambda_u}]}\right)\ [\mu\text{m}\ ].$$

With the effective radius known the optical depth and mass loading can be found using Equations (B.3) and (B.1). The effect of scattering can be included using an iterative method that guesses r_{eff} to calculate R_λ and then arrives at a new r_{eff}.

B.4 Sources of Error

An extensive list of the sources of error to the estimation of the mass loading is included. The error of the mass loading u due to a parameter α is defined as

$$\Delta u_\alpha = \frac{\partial u}{\partial \alpha}\Delta\alpha. \tag{B.6}$$

Note that the partial derivatives should be computed numerically. The total error to the mass loading Δu can then be found from the individual contributions of error as

$$\Delta u = \sqrt{\sum_\alpha (\Delta u_\alpha)^2}. \tag{B.7}$$

A compilation of the sources of error to the mass loading is given below in Table B.1. Typical values are given for each parameter. Note that the effect of scattering is not included.

Table B.1: Typical Error of Mass Loading

Parameter	(α)	**Typical Value**	**Error** ($\Delta\alpha$)	**Contribution** (Δu_α)
Ground Emmisivity;	ε_g	0.95	0.025	0.019 g/m^2
Incident Radiance;	J_{rec,λ_L}	2.013 W/(m^2 sr μm)	0.0677 W/(m^2 sr μm)	0.201 g/m^2
	J_{rec,λ_U}	2.405 W/(m^2 sr μm)	0.0689 W/(m^2 sr μm)	0.148 g/m^2
Cloud Temperature;	T_c	240 K	5 K	0.204 g/m^2
Ground Temperature;	T_g	300 K	5 K	0.009 g/m^2
Pumice Density;	ρ_v	2.6×10^6 g/m^3	0.05×10^6 g/m^3	0.049 g/m^2
Effective Radius;	r_{eff}	2 μm	0.2 μm	0.254 g/m^2

B.4.1 Effect of IR Camera Calibration

The above parameters are used to predict a mass loading u of 2.539 g/m^2 with a mass loading uncertainty Δu of ± 0.414 g/m^2. This assumes a uniform particle size distribution and that scattering is ignored. Other assumptions on parameters are shown in Table B.1. This gives a relative uncertainty of 16% with the radius particle uncertainty as the largest contributor to the mass loading uncertainty. Note that the above spectral radiance uncertainties correspond to a sensor noise equal to the quantification limit.

If the standard noise level is used without oversampling or filtering this mass loading uncertainty is increased to ± 2.121 g/m^2 and the error is almost as large as the predicted mass, with a relative uncertainty of 84%. However, if spacial filtering is used to reduce the spectral noise to 0.220 $W/(m^2\ sr\ \mu m)$ and 0.203 $W/(m^2\ sr\ \mu m)$ for the lower and upper spectral bands respectively, this mass loading uncertainty is reduced to 0.847 g/m^2. This gives a relative mass loading uncertainty of 33%. Therefore, the Quark camera must use either image filtering or oversampling to provide spectral radiance noise levels low enough to predict the mass loading of volcanic ash clouds. The relative uncertainty of volcanic ash mass loading is shown below in Table B.2. Note that the spectral radiance uncertainty is the main contributor to mass loading error, except in the case of the oversampling limit where the pumice density uncertainty becomes the most important contributor.

Table B.2: Mass Loading Error for Different Noise Reduction Methods

Method	**Mass Loading Error (%)**
Standard Noise	84
Image Filtering	33
Oversampling Limit	16

B.5 Detection Range of BTD Method

The detection range of the BTD method depends on the maximum and minimum detectable optical depth of the cloud. The detectable range of the optical depth can be estimated graphically as shown below in Figure B.3 and assuming a

temperature error of ± 0.5 °C. This gives a maximum optical depth of 3.0 and a minimum optical depth of 0.2.

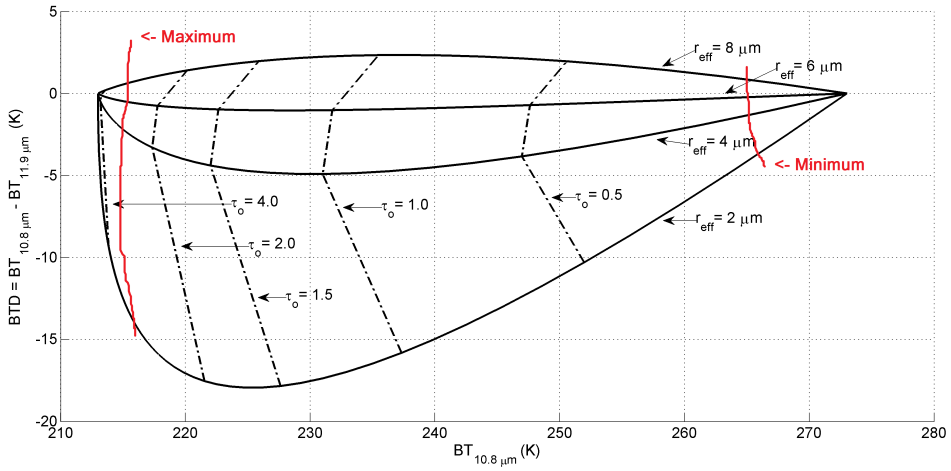

Figure B.3: Maximum and Minimum Range of Detection of BTD Method

The detectable range of the effective particle radius is between 1 μm and 5 μm. From here the detectable range of the effective mass loading can be calculated using Equation B.1. The detectable range of the mass density is calculated assuming a cloud depth of 1 km to give

$$0.35\ \mathrm{g/m^2} \leq u \leq 26\ \mathrm{g/m^2},$$

and

$$0.00035\ \mathrm{g/m^3} \leq \rho_c \leq 0.026\ \mathrm{g/m^3}.$$

Appendix C
Electronic System Design

C.1 Introduction

This section reviews the electronic design used for interfacing with the Quark camera, controlling the servo motor, and measuring the temperature of the on-board black body source. One electronic design goal it to provide reliable power from the UAV to the Raspberry Pi and the Quark camera. A second goal is to provide communication between the Raspberry Pi acting as the central hub and the various branches including the UAV, the Quark camera and the PIC microcontroller used for controlling the filter wheel. An overall block diagram with circuit components of this design is presented below in Figure C.1.

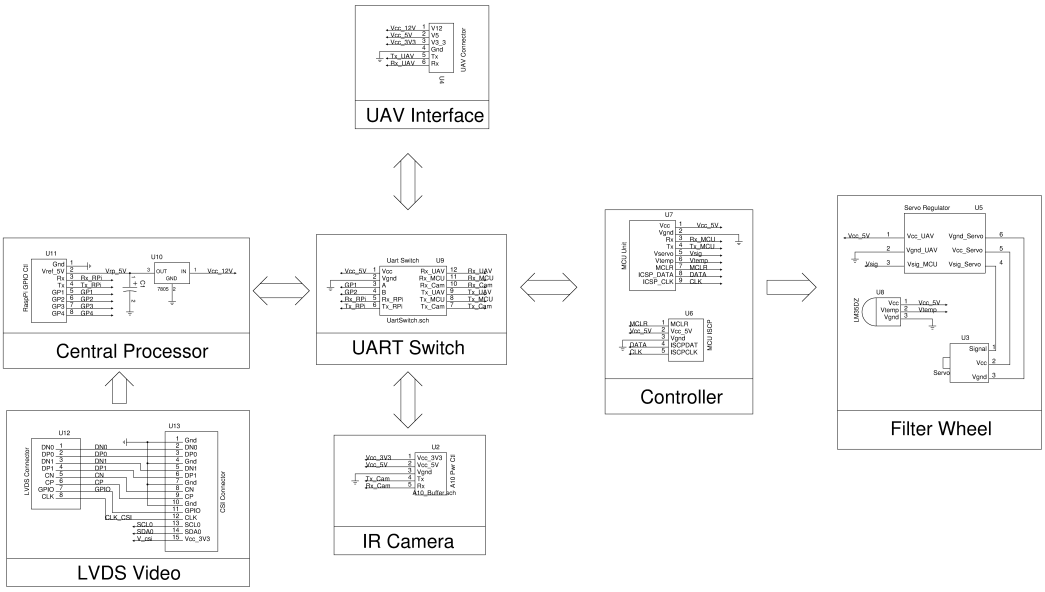

Figure C.1: Overall Schematic of Electronic Control Board

C.2 UAV Connection

A primary constraint to the electronic interface design is what is available from the UAV in terms of power and communication. Steven Kibler, a systems engineer at the Alaska Center for Unmanned Aircraft Systems Integration (ACUSAI), indicated the basic available interface to consist of power at 12 V, 5 V, and 3.3 V along with a basic communication interface such as the universal asynchronous receive

transmit (UART) interface. In addition, the communication link of the UAV is limited and only image snap-shots can be transmitted. The actual data would need to be extracted from the SD card once the UAV is recovered.

C.3 Quark Camera Connection

The electronic interface to the IR camera is shown below in Figure C.2. A 220 μF capacitor is added for limiting voltage ripple. The analog video can be transmitted with an added coax cable that is terminated with an RCA video connector. Since the Quark uses an RS-232 communication interface the UART channel must be inverted to operate correctly. Two 2.2 kΩ resistors are provided to protect the communication channel of the Quark.

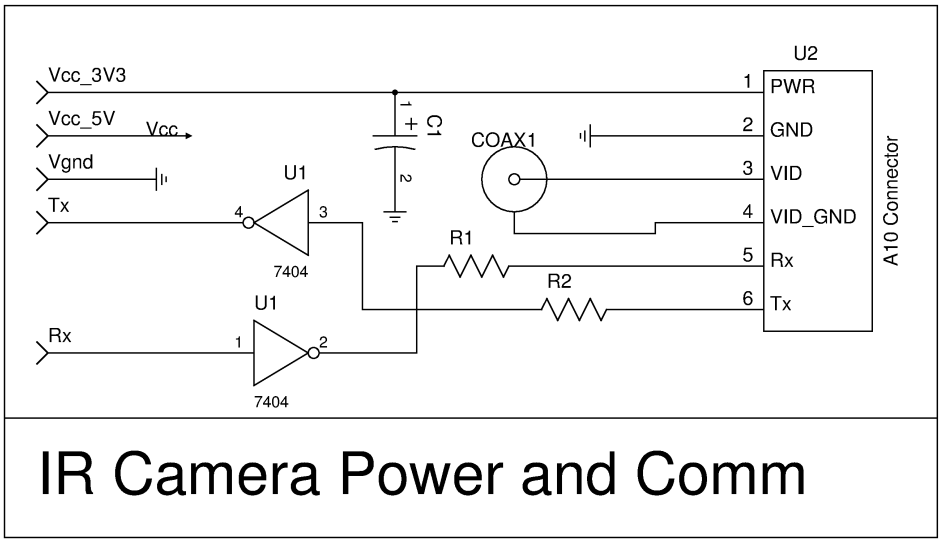

Figure C.2: Schematic of Electronic Interface to Quark Camera

C.4 Servo Motor Controller

The servo motor draws a large amount of current during motor start-up. If the servo motor is directly connected to the 5 V rail the voltage will drop enough to reset the microcontroller. To avoid this a filter was constructed using two capacitors and a large inductor as shown in Figure C.3. In addition, the servo motor requires a pulse width modulated (PWM) to set the required position of the motor. This draws more current than a microcontroller can supply and therefore a non-inverting buffer was constructed using a NPN transistor and resistor. The servo

selected was the GWS S125 1T 2BB that was capable of a full turn of rotation.

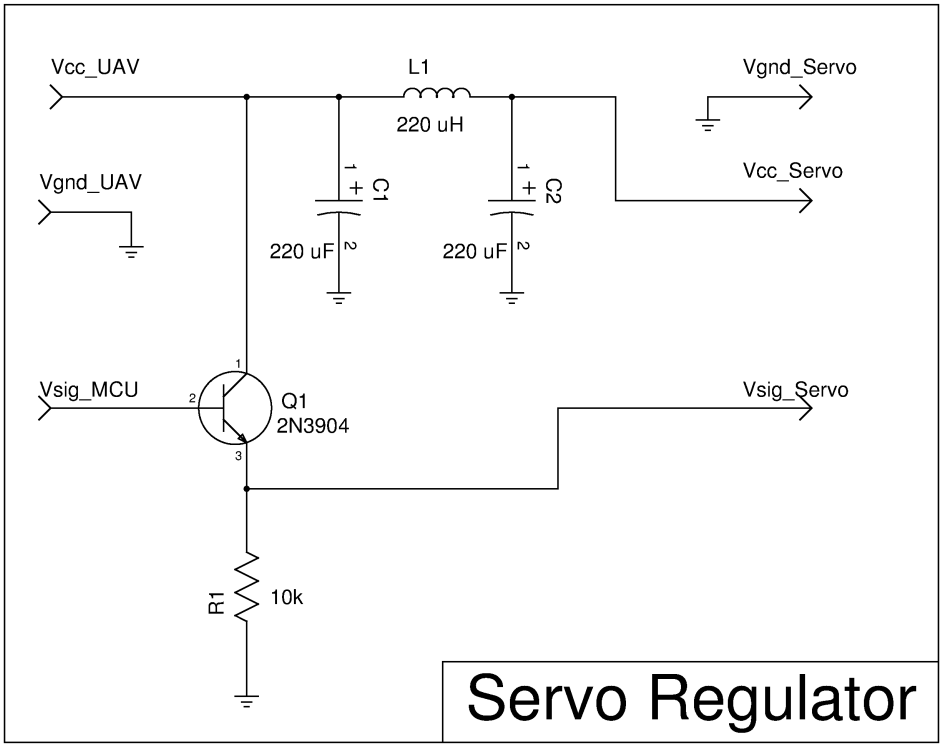

Figure C.3: Schematic of Servo Motor Regulator

The microcontroller selected was the Microchip PIC 16F722 because of its simplicity of use. An external 20 MHz crystal provides the clock signal that is high enough in frequency to send PWM signal with accurate pulse widths. This microcontroller also has an ADC that samples the on-board BBS thermal sensor output to provide a temperature that is accurate to within ± 0.2 K. The controller will read commands over the UART channel to either change the filter position or report the BBS temperature. In an idle state the microcontroller will transmit a constant PWM signal to ensure the filter wheel does not rotate.

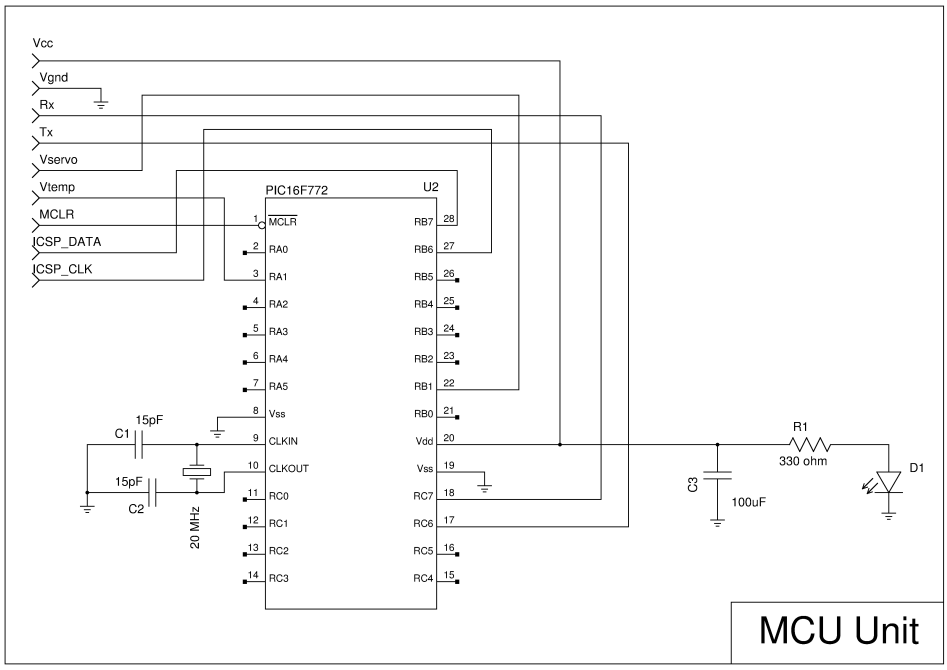

Figure C.4: Schematic of PIC Microcontroller Connection

C.5 UART Switch

The UART switch is used to connect the Raspberry Pi communication channel to the UAV, the Quark camera, or the microcontroller as needed. This consists of the 74153 multiplexer and the 74155 demultiplexer. A voltage divider was added to the Raspberry Pi ports for protection to ensure a maximum voltage of less than 3.3 V. Two general purpose input/output ports are used, denoted as A and B, to control which channel the UART switch is selecting.

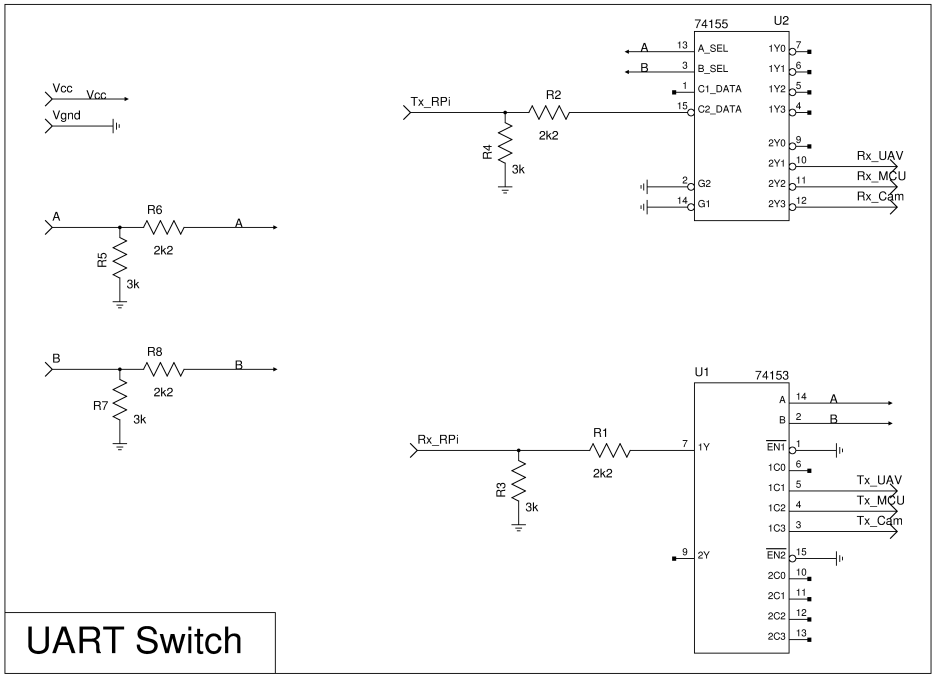

Figure C.5: Schematic of UART Switch

C.6 Board Layout

The control board was proto-typed in house as a two sided 62 mil FR4 board. Images of the top and bottem layers of the board is presented below in Figure C.6.

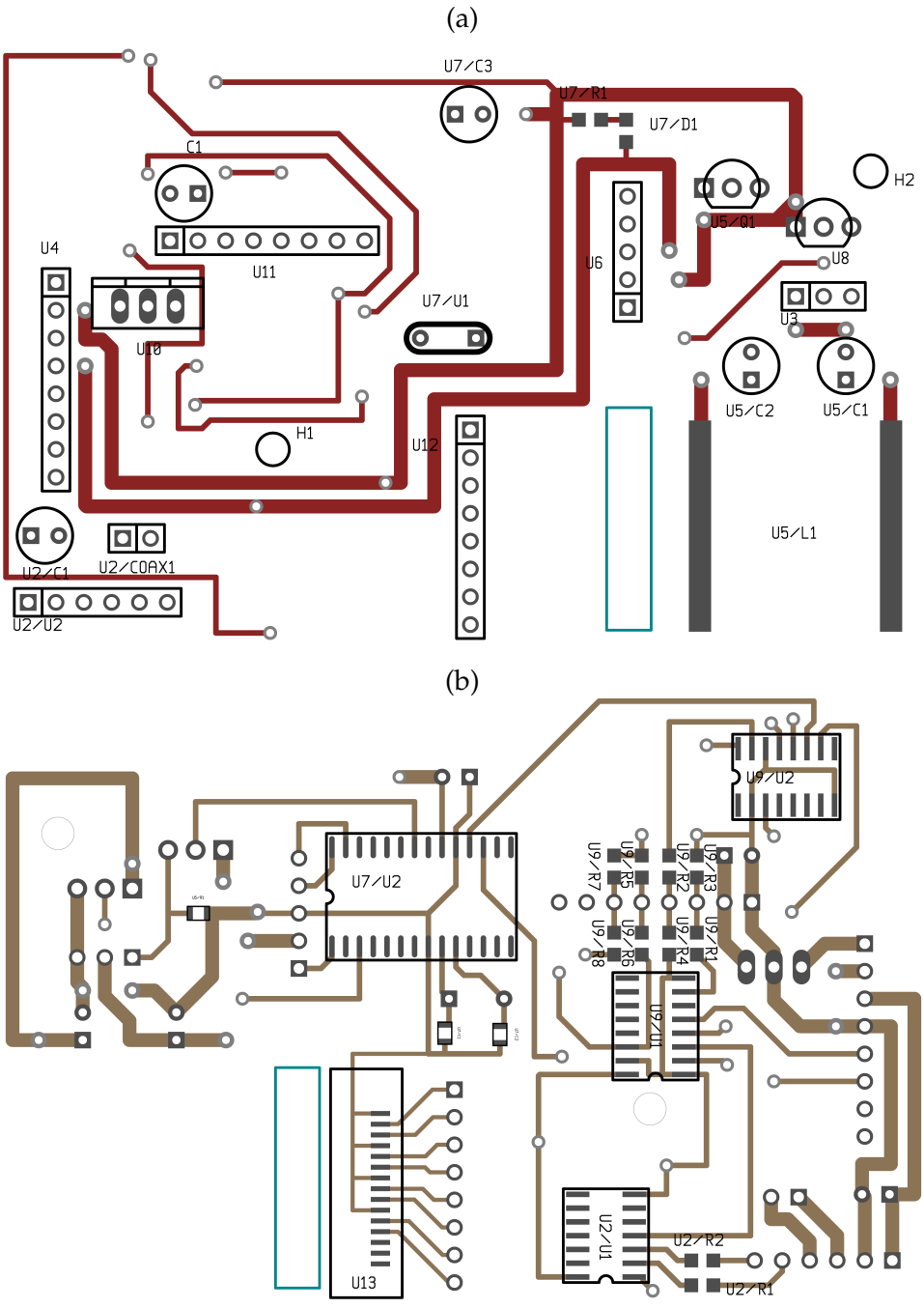

Figure C.6: Physical Layout of Top (a) and Bottom (b) Layers

C.7 Power Supply Concerns

This imaging system has two large consumers of power: the Raspberry Pi with 400 mA at 5 V and the Quark camera with 350 mA at 3.3 V. The Quark camera

in particular has a very low tolerance of voltage ripple with a minimum voltage required of 3.2 V. If the input voltage from the UAV is inadequate, then a DC-DC converter will be required to provide a consistent voltage regardless of the voltage level of the UAV. The Raspberry Pi was found to be too sensitive to ripple voltage to be connected to the standard 5 V rail and was therefore given a devoted 5 V power supply regulated from the 12 V supply. A more adequate power supply for both the Raspberry Pi and Quark camera should be considered in an actual implementation for both reliability and power efficiency.

C.8 Conclusions

A basic electronic interface design was reviewed with the goal to provide power and communication between the separate devices. The UART communication interface was used to communicate between the various devices. A filter was required to prevent excessive voltage ripple on the 5 V power supply. Further development of the power supply to the Raspberry Pi and Quark camera is required for practical UAV or spacecraft applications.